A limited-area dual-resolution hybrid variational-ensemble data assimilation system for the WRF model

Craig S. Schwartz*, Zhiquan Liu, Xiang-Yu Huang, and Ying-Hwa Kuo

National Center for Atmospheric Research, Boulder, Colorado, USA

NCAR is sponsored by the National Science Foundation

*Corresponding author address:

Craig Schwartz, National Center for Atmospheric Research (NCAR), 3090 Center Green Drive, Boulder, Colorado 80301

Email: schwartz@ucar.edu

ABSTRACT

Dual-resolution (DR) hybrid variational-ensemble analysis capability was implemented within the community Weather Research and Forecasting (WRF) model data assimilation (DA) system. The DR hybrid system combines a high-resolution (HR) background, flow-dependent background error covariances (BECs) derived from a low-resolution (LR) ensemble, and observations to produce a deterministic HR analysis. As DR systems do not require a HR ensemble, they are computationally cheaper than a single-resolution (SR) hybrid configuration, where both the background and ensemble have equal resolutions.

Single-observation tests were performed to document some characteristics of DR hybrid analyses. Additionally, the DR hybrid system was evaluated in a continuously cycling framework, where a new DR hybrid analysis was produced every 6-hrs over a ~3.5 week period. In our DR configuration, the deterministic backgrounds and analyses had 15-km horizontal grid spacing, but the 32-member WRF-based ensemble providing flow-dependent BECs for the hybrid had *45-km* horizontal grid spacing. The DR hybrid analyses initialized 72-hr WRF model forecasts that were compared to forecasts initialized by a SR hybrid system where both the ensemble and background had 15-km horizontal grid spacing. The SR and DR hybrid systems were coupled to an ensemble adjustment Kalman filter (EAKF) that updated the ensembles each DA cycle.

On average, forecasts initialized from 15-km DR hybrid analyses performed similarly as those initialized by 15-km SR hybrid analyses. These results suggest that using LR ensemble BECs in combination with a HR background is justifiable, which permits considerable computational savings.

1. Introduction

Ensemble-based data assimilation (DA) methods, such as the ensemble Kalman filter (EnKF; Evensen 1994; Burgers et al. 1998; Houtekamer and Mitchell 1998), have become popular alternatives to traditional variational DA approaches. EnKFs use short-term ensemble forecasts to calculate flow-dependent, multivariate background error covariances (BECs), contrasting the static, isotropic BECs typically employed in three-dimensional variational (3DVAR; e.g., Barker et al. 2004) DA.

Flow-dependent BECs can also be introduced into DA systems without an EnKF. Specifically, ensemble-derived BECs can be incorporated within a variational framework in a "hybrid" variational-ensemble DA algorithm (e.g., Hamill and Snyder 2000; Lorenc 2003; Buehner 2005; Wang et al. 2008a; Zhang et al. 2009; Wang 2010; Clayton et al. 2012; Kuhl et al. 2013). Moreover, hybrid paradigms permit flexibility regarding how much the total BECs are weighted toward ensemble and static (i.e., 3DVAR) contributions. Although hybrid analyses are deterministic, since an ensemble is required to provide flow-dependent BECs, hybrid systems are often coupled with EnKFs that update the ensemble each DA cycle (e.g., Wang et al. 2008a,b; Hamill et al. 2011; Wang 2011; Zhang and Zhang 2012; Gao et al. 2013; Schwartz et al. 2013; Wang et al. 2013; Zhang et al. 2013; Pan et al. 2014; Schwartz and Liu 2014).

The hybrid method has shown great promise for initializing numerical weather prediction (NWP) model forecasts. It has been demonstrated that hybrid approaches typically initialize comparable or better forecasts than purely variational methods that do not incorporate ensemble BECs and can outperform forecasts initialized by standalone EnKFs (e.g., Buehner 2005; Wang et al. 2008b; Buehner et al. 2010; Hamill et al. 2011;

Wang 2011; Li et al. 2012; Zhang and Zhang 2012; Wang et al. 2013; Zhang et al. 2013; Schwartz et al. 2013; Pan et al. 2014; Schwartz and Liu 2014). Additionally, the hybrid technique can be easily implemented in pre-existing variational DA systems and may produce similar results as EnKFs but with a smaller ensemble (e.g., Wang et al. 2007a, Zhang et al. 2013; Pan et al. 2014). Moreover, as the hybrid employs model-space covariance localization, assimilation of non-local observations, such as satellite radiances, may be more effective in hybrid frameworks than in EnKFs that use observation-space localization (Campbell et al. 2010). Given these attractive features and successful hybrid-initialized forecasts, the National Centers for Environmental Prediction (NCEP) Global Forecast System (GFS) model is now initialized with a hybrid-3DVAR system (Wang et al. 2013) and the United Kingdom Met Office uses a four-dimensional variational (4DVAR; e.g., Courtier et al. 1994) hybrid to initialize their global model (Clayton et al. 2012).

Many studies have described limited-area hybrid systems that employ a "single resolution" (SR) configuration, where the ensemble providing flow-dependent BECs has the same resolution as the deterministic background and analysis (e.g., Wang et al. 2008b; Wang 2011; Li et al. 2012; Zhang and Zhang 2012; Zhang et al. 2013; Schwartz et al. 2013; Schwartz and Liu 2014; Pan et al. 2014). However, a "dual-resolution" (DR) hybrid analysis can be produced that combines a high-resolution (HR) background with a low-resolution (LR) ensemble to produce a HR analysis, obviating the need for a costly HR ensemble. As the most expensive component of ensemble DA systems involves advancing an ensemble of forecasts between analyses, if hybrid analyses using flow-dependent BECs provided by a LR ensemble can initialize forecasts with comparable quality as those initialized by hybrid analyses that ingest HR perturbations, considerable computational savings can be realized. Given these savings—and out of practical necessity—several global hybrid DA configurations have employed DR approaches (e.g., Buehner et al. 2010; Hamill et al. 2011; Clayton et al. 2012; Kuhl et al. 2013), including the operational NCEP GFS 3DVAR-hybrid system (as noted in Wang et al. 2013).

We note that use of multiple resolutions within DA systems is not confined to hybrid methods. Multiple resolutions are commonly employed in incremental 4DVAR (Courtier et al. 1994) systems, where a HR nonlinear model is used to calculate innovations based on a HR guess field and define a trajectory about which LR tangent linear and adjoint models are formulated. Moreover, Gao and Xue (2008) described an ensemble DA system that updated a deterministic HR background using BECs derived from a LR ensemble. The HR forecast evolved independently of the LR ensemble and BECs calculated in LR space were used to update both the HR background and LR ensemble members. Gao and Xue (2008) reported encouraging results using this approach and noted that it afforded large computational savings compared to employing a SR DA system. Additionally, Rainwater and Hunt (2013) discussed the merits of a DR EnKF where the ensemble was a mixture of HR and LR members.

However, Gao and Xue (2008) assimilated simulated radar observations in an idealized case study of a supercell and Rainwater and Hunt (2013) assimilated synthetic observations with a simple, idealized model. Thus, investigations regarding DR and SR applications for ensemble DA systems are needed for real-data cases. Moreover, the performance of DR versus SR hybrid analysis/forecast systems has not been thoroughly documented for either global or regional applications.

This paper describes the implementation of a DR hybrid analysis system within the community Weather Research and Forecasting (WRF; Skamarock et al. 2008) model DA system (WRFDA; Barker et al. 2012) that is designed for limited-area modeling applications. We describe the DR hybrid formulation and present single-observation tests to understand basic properties of DR analyses. Additionally, we assimilate real observations with a DR hybrid system that combined a 15-km background and a 45-km ensemble in a continuously cycling configuration over a ~3.5 week period. The DR analyses initialized 72-hr WRF model forecasts over southeast Asia. Similarly-configured 15-km SR hybrid analyses and forecasts were also generated and compared to those produced by the DR system. The DR and SR hybrid systems were coupled to an ensemble adjustment Kalman filter (EAKF; Anderson 2001, 2003) from the Data Assimilation Research Testbed (DART; Anderson et al. 2009) software that updated the ensemble each DA cycle. This work also extends that of Schwartz et al. (2013; hereafter S13), who examined 45-km 3DVAR and SR hybrid analysis/forecast systems over the same region and time period.

Section 2 describes the DR hybrid algorithm and its practical implementation, while section 3 details the WRF configurations and DA settings. The experimental design is presented in section 4 and section 5 briefly discusses the observations. Results regarding single-observation experiments are described in section 6, section 7 examines analyses and forecasts produced by continuously cycling DR and SR hybrid systems that assimilated real observations, and we conclude in section 8.

2. The WRFDA dual-resolution hybrid system

a. Mathematical formulation

WRFDA's hybrid algorithm (Wang et al. 2008a) is an extension of its 3DVAR formulation (Barker et al. 2004). Thus, our description of the DR hybrid starts with the 3DVAR cost-function. For simplicity, we consider the formulation for a single outer-loop (OL; Courtier et al. 1994) analysis, which is sufficient to illustrate implementation of the DR hybrid.

In 3DVAR, a best-fit analysis is calculated considering observations and a background field, typically a short-term model forecast. Associated with the background and observations are their error characteristics. Given the background, observations, and errors, the 3DVAR analysis vector ($\mathbf{x}$) can be determined by iteratively minimizing a scalar cost-function (J) given by

$$J(\mathbf{x}) = \frac{1}{2}(\mathbf{x}-\mathbf{x_b})^{\mathrm{T}}\mathbf{B}^{-1}(\mathbf{x}-\mathbf{x_b}) + \frac{1}{2}[H(\mathbf{x})-\mathbf{y}]^{\mathrm{T}}\mathbf{R}^{-1}[H(\mathbf{x})-\mathbf{y}], \qquad (1)$$

where $\mathbf{x_b}$ denotes the background vector, $\mathbf{y}$ is a vector of observations, and H is the potentially non-linear "observation operator" that interpolates grid point values to observation locations and transforms model-predicted variables to observed quantities. Matrices $\mathbf{B}$ and $\mathbf{R}$ contain the background and observation error covariances, respectively. By linearizing $H(\mathbf{x})$ about $\mathbf{x_b}$, Eq. (1) can be written in "incremental form" (Courtier et al. 1994) as

$$J(\delta\mathbf{x}) = \frac{1}{2}(\delta\mathbf{x})^{\mathrm{T}}\mathbf{B}^{-1}(\delta\mathbf{x}) + \frac{1}{2}(\mathbf{H}\delta\mathbf{x}-\mathbf{y}')^{\mathrm{T}}\mathbf{R}^{-1}(\mathbf{H}\delta\mathbf{x}-\mathbf{y}'), \qquad (2)$$

where $\delta\mathbf{x} = \mathbf{x} - \mathbf{x_b}$ is the analysis increment vector, $\mathbf{y}' = \mathbf{y} - H(\mathbf{x_b})$ is the innovation vector, and matrix $\mathbf{H}$ is the linearized version of H.

In Eq. (2), $\delta\mathbf{x}$ is a vector of length n, consisting of WRFDA's five control variables: stream function, pseudo relative humidity, and unbalanced velocity potential, temperature, and surface pressure (Barker et al. 2004). To produce hybrid analyses, BECs from an N-member ensemble are incorporated into the cost function using the extended control variable approach (Lorenc 2003; Wang et al. 2008a). First, the total analysis increment is partitioned as

$$\delta\mathbf{x} = \mathbf{x}_1 + \sum_{i=1}^{N} \mathbf{a}_i \circ \mathbf{x}_i' , \tag{3}$$

where $\mathbf{x}_1$ is the n-dimensional analysis increment vector associated with the static BECs (i.e., 3DVAR) and the second term on the right hand side (RHS) of Eq. (3) is the increment associated with the ensemble BECs. The vector $\mathbf{x}_i'$ is the perturbation of the ith prior (before assimilation) ensemble member about the prior ensemble mean normalized by $(N\text{-}1)^{1/2}$, vector $\mathbf{a}_i$ is a control variable (Lorenc 2003) that determines weighting for the ensemble perturbations, and the symbol $\circ$ denotes a Schur product (element by element multiplication).

Each $\mathbf{x}_i'$ is a vector of length n_l, where $n_l \leq n$. Necessarily, each $\mathbf{a}_i$ is also a vector of length n_l. In a SR hybrid system, $n_l = n$ and the ensemble and background are at identical resolutions. But, in a DR hybrid system, $n_l < n$, meaning the ensemble is at coarser resolution than the background. Therefore, DR hybrid analyses have fewer extended control variables (i.e., $\mathbf{a}$) than SR hybrid analyses.

Following Wang (2010), we define n_l x n_l matrix $\mathbf{d}_i = diag(\mathbf{x}_i')$, where $diag$ is an operator that converts vector $\mathbf{x}_i'$ into diagonal matrix $\mathbf{d}_i$, whose pth diagonal element is the pth element of $\mathbf{x}_i'$. Further, let $\mathbf{D}$ be the n_l x (Nn_l) matrix defined as $\mathbf{D} = [\mathbf{d}_1\ \mathbf{d}_2\ \mathbf{d}_3 \ldots \mathbf{d}_N]$, and concatenate each $\mathbf{a}_i$ to form vector $\mathbf{a}$ of length (Nn_l):

$$\mathbf{a} = \begin{bmatrix} \mathbf{a}_1 \\ \mathbf{a}_2 \\ \mathbf{a}_3 \\ \vdots \\ \mathbf{a}_N \end{bmatrix}. \tag{4}$$

Then,

$$\delta\mathbf{x} = \mathbf{x}_1 + \mathbf{Da}\ . \qquad (5).$$

Eqs. (3) and (5) are identical, but Eq. (5) is simpler because it does not contain summations or Schur products. When the ensemble and background are at the same resolution (SR hybrid), Eq. (5) is valid since $n_l = n$ and both terms on the RHS of Eq. (5) are n-dimensional vectors. However, if $n_l < n$, as in a DR application, Eq. (5) is *invalid* since the two terms on the RHS side of Eq. (5) are vectors of different lengths. Thus, for DR applications, interpolation of one term is needed. Since we wish to produce a HR analysis, we introduce an interpolation operator **L** to interpolate the quantity **Da** from LR to HR space.

Strictly, **L** is an n x n_l matrix, where each row of **L** specifies how a single HR grid point is related to each LR grid point. While theoretically, **L** could be any interpolation method, we defined **L** as the same bilinear interpolation operator used to interpolate the model state to observation locations in H to make use of existing code in WRFDA.

Introducing **L** into Eq. (5) gives

$$\delta\mathbf{x} = \mathbf{x}_1 + \mathbf{LDa}\ . \qquad (6).$$

For a SR application ($n_l = n$), $\mathbf{L} = \mathbf{I}$, the identity matrix, and Eq. (5) is recovered. Thus, Eq. (6) is a general expression for the total increment since it is valid even if $n \neq n_l$.

The corresponding cost function that is minimized with respect to $\mathbf{x}_1$ and $\mathbf{a}$ to obtain the hybrid analysis increment is

$$\begin{aligned} J(\mathbf{x}_1,\mathbf{a}) &= \beta_1 \frac{1}{2}(\mathbf{x}_1)^{\mathbf{T}}\mathbf{B}^{-1}(\mathbf{x}_1) \\ &+\beta_2 \frac{1}{2}(\mathbf{a})^{\mathbf{T}}\mathbf{A}^{-1}\mathbf{a} \\ &+\frac{1}{2}(\mathbf{H}\delta\mathbf{x}-\mathbf{y}')^{\mathbf{T}}\mathbf{R}^{-1}(\mathbf{H}\delta\mathbf{x}-\mathbf{y}') \end{aligned}, \tag{7}$$

where $\delta\mathbf{x}$ is given by Eq. (6), and $\mathbf{A}$ is an (Nn_l) x (Nn_l) block diagonal matrix that controls the spatial correlation of $\mathbf{a}$, effectively performing localization of the ensemble BECs (Wang et al. 2007b). Note that $\mathbf{A}$ is in the ensemble space, while $\mathbf{B}$ is in the space of the background. Moreover, $\mathbf{A}$ is typically defined with long localization length scales, which constrains $\mathbf{a}$ to be spatially smooth (e.g., Wang 2010) and motivates the potential for successful DR hybrid systems. The terms β_1 and β_2 determine how much weight is given to the ensemble and static BECs and are constrained such that

$$\frac{1}{\beta_1}+\frac{1}{\beta_2}=1. \tag{8}$$

Eq. (7) is minimized by taking its gradient with respect to $\mathbf{x}_1$ and $\mathbf{a}$ and equating with zero, which yields

$$\nabla_{\mathbf{x}_1} J = \beta_1\mathbf{B}^{-1}\mathbf{x}_1 + \mathbf{H}^{\mathbf{T}}\mathbf{R}^{-1}(\mathbf{H}\delta\mathbf{x}-\mathbf{y}') = 0 \tag{9}$$

and

$$\nabla_{\mathbf{a}} J = \beta_2\mathbf{A}^{-1}\mathbf{a} + \mathbf{D}^{\mathbf{T}}\mathbf{L}^{\mathbf{T}}\mathbf{H}^{\mathbf{T}}\mathbf{R}^{-1}(\mathbf{H}\delta\mathbf{x}-\mathbf{y}') = 0\,. \tag{10}$$

In Eq. (10), $\mathbf{L}^{\mathbf{T}}$ is the adjoint of $\mathbf{L}$, which transforms $\mathbf{H}^{\mathbf{T}}\mathbf{R}^{-1}(\mathbf{H}\delta\mathbf{x}-\mathbf{y}')$ from HR to LR space. Within the context of variational minimization, for DR hybrid applications, each iteration, $\mathbf{L}^\mathbf{T}$ is applied to $\mathbf{H}^\mathbf{T}\mathbf{R}^{-1}(\mathbf{H}\delta\mathbf{x}-\mathbf{y}')$ and $\mathbf{L}$ is applied to $\mathbf{Da}$. It is unclear how much representativeness error is introduced by interpolating quantities from LR to HR (and vice-versa) each iteration, although representativeness errors should increase as the ratio of LR to HR horizontal grid spacing increases. However, since the interpolated quantities are the ensemble contribution to the increment ($\mathbf{Da}$) and the adjoint vector $[\mathbf{H}^\mathbf{T}\mathbf{R}^{-1}(\mathbf{H}\delta\mathbf{x}-\mathbf{y}')]$, which are spatially smooth compared to $\mathbf{x_b}$, these representativeness errors may be somewhat diminished.

b. Practical considerations

WRFDA can perform DR hybrid analyses for any valid nested configuration of the WRF model, offering users great flexibility to produce HR analyses over a domain of interest without the need for an expensive HR ensemble. To produce a DR analysis, a valid nested WRF domain is created, with a HR "child" grid nested within a LR "parent" grid (Fig. 1). WRF model fields on the HR grid provide the background for a DR analysis, while the ensemble BECs are provided using ensemble fields on the parent grid. WRFDA uses solely the portion of the LR parent grid co-located with the HR child grid to compute the ensemble-derived BECs for a DR analysis.

Currently, the parent domain can only provide ensemble BECs for a child domain nested one level down. Thus, the 45-km domain (d01) in Fig. 1a can directly provide ensemble BECs for a 15-km (d02) hybrid analysis but not for a 5-km (d03) hybrid analysis. However, an ensemble on the 15-km grid (d02) could provide BECs for a 5-km (d03) hybrid analysis. Additionally, WRFDA can only produce an analysis for one domain at a time. Thus, for a nested configuration where the parent has two children

(Fig. 1b), while the 45-km domain (d01) can provide the ensemble BECs for hybrid analyses on both the 15-km (d02) and 5-km (d03) domains, WRFDA must be run twice.

The DR analysis does not update any field on the parent grid. So, if a hybrid analysis on the LR parent grid is desired, a LR ensemble and deterministic background must be available. Furthermore, if an ensemble is available on the child grid, a SR hybrid analysis can be performed on the HR grid. The remainder of this paper focuses on results produced by various hybrid systems that employ both DR and SR configurations.

3. WRF model and data assimilation configurations

The WRF model and DA configurations were very similar to those in S13. Thus, generally brief descriptions follow.

a. Forecast model

Weather forecasts were produced by version 3.3.1 of the non-hydrostatic Advanced Research WRF (Skamarock et al. 2008) model. All experiments ran over a one-way nested computational domain encompassing the western Pacific Ocean and eastern Asia (Fig. 2). The horizontal grid spacing was 45-km (222 x 128 grid points) in the outer domain and 15-km (316 x 274 grid boxes) in the inner nest. Both domains were configured with 45 vertical levels and a 30 hPa top. The time step was 180 seconds in the 45-km domain and 60 seconds in the 15-km nest. GFS forecasts provided lateral boundary condition (LBC) forcing for the 45-km domain every 6-hrs and the 45-km domain provided LBCs for the 15-km nest. The same physical parameterizations as in S13 were used in both domains and are listed in Table 1.

b. EAKF and hybrid data assimilation settings

The hybrid uses an ensemble of short-term forecasts to incorporate flow-dependent BECs in the variational cost-function [i.e., Eq. (7)] and the ensemble needs to be updated when new observations are available. The EAKF from the DART was used to update a 32-member WRF-based ensemble. To reduce spurious correlations due to sampling error, localization forced EAKF analysis increments to zero ~1280-km from an observation in the horizontal and ~10-km in the vertical. Adaptive inflation (Anderson 2009) was applied immediately before prior model-simulated observations were computed to maintain ensemble spread. A stochastic kinetic-energy backscatter scheme (Shutts 2005; Berner et al. 2009) was applied during the WRF model advances between each EAKF analysis to further preserve spread.

Localization was also applied in the hybrid to limit the spatial extent of the ensemble contribution to the analysis increments. Horizontal localization of approximately the same length-scale in DART was applied in the hybrid. Vertical localization length-scales in the hybrid increased with height (see S13 for more information).

Static 45- and 15-km BECs used in the hybrid algorithm were constructed using the "NMC Method" (Parrish and Derber 1992) from WRF forecasts produced over this domain for multiple months and used operationally by the Taiwan Central Weather Bureau (CWB), as described by S13. Three OLs were used in the hybrid minimization. As in S13, hybrid BECs were weighted 75% toward the ensemble contribution and 25% toward the static (i.e., 3DVAR) component. We also weighted the BECs equally between the ensemble and static contributions and achieved similar results. Limited sensitivity to BEC weightings in SR hybrid configurations has also been noted elsewhere (e.g., Wang 2011; Wang et al. 2013; Zhang et al. 2013), but Wang et al. (2013) stated that in preliminary testing, forecasts were improved in a global DR hybrid-3DVAR system when the total BECs were weighted equally between the static and ensemble contributions compared to when ensemble BECs provided the total BECs (i.e., no static contribution).

4. Experimental design

Three experiments were designed to investigate the performance of DR and SR hybrid analysis/forecast systems. All experiments began at 0000 UTC 4 September by interpolating the deterministic 0.5 x 0.5 degree NCEP GFS analysis onto the nested computational domain (Fig. 2). The initial 45-km ensemble was constructed at this time by taking Gaussian random draws with zero mean and static BECs (Barker 2005; Torn et al. 2006) and adding them to the GFS field. LBCs for the ensemble system were perturbed similarly. The initial 15-km ensemble was produced by downscaling the perturbed 45-km fields onto the 15-km grid, similar to Ha and Snyder (2014).

The deterministic and ensemble fields produced at 0000 UTC 4 September initialized 6-hr WRF forecasts which served as backgrounds for the first hybrid and EAKF analyses at 0600 UTC 4 September. Thereafter, the EAKF and hybrid configurations cycled continuously until 0000 UTC 28 September, and a new analysis was produced every 6-hrs. The background for DA was always the previous cycle's 6-hr forecast. Nested 45-/15-km 72-hr WRF model forecasts were initialized every 6-hrs from hybrid analyses between 1800 UTC 8 and 0000 UTC 28 September (inclusive; 78 total forecasts). Identical to S13, digital filter initialization (DFI; Lynch and Huang 1992, Huang and Lynch 1993) using a twice-DFI scheme and the Dolph filter (Lynch 1997) with a 2-hr backwards integration was applied to all 72-hr forecasts, but not during the 6-hr cycling between analyses. S13 examined this same period and employed an identical experimental design, but they only produced 45-km SR hybrid analyses.

Although DART can update multiple WRF domains in one step (e.g., Ha and Snyder 2014), if multiple domains are simultaneously analyzed, analysis variables from one domain may impact analysis variables in another. We wanted to keep the 45- and 15-km ensemble systems separate to cleanly isolate sensitivity of using HR and LR perturbations in hybrid analyses, so, when 15-km EAKF analyses were required, the EAKF produced separate, independent 45- and 15-km analyses.

The 45- and 15-km prior ensembles produced by cycling EAKF-WRF systems were used as input to hybrid analyses. Like the EAKF, all hybrid experiments produced separate, independent 45- and 15-km analyses. The three hybrid experiments differed by the resolution of the ensemble perturbations ingested by the *15-km* hybrid analyses (which determined whether 15-km EAKF analyses and *ensemble* forecasts were needed) and whether the EAKF analysis ensemble was re-centered about the hybrid analysis (e.g., Zhang et al. 2013; Wang et al. 2013; Pan et al. 2014):

1) “Hybrid_SR” : Separate, independent SR 45- and 15-km hybrid analyses were produced each DA cycle. The 45-km hybrid analyses incorporated BECs from the cycling 45-km EAKF-WRF ensemble system, while the 15-km hybrid analyses used BECs from the cycling 15-km EAKF-WRF ensemble system. Since 15-km ensembles

were needed for the 15-km SR hybrid, each ensemble member was advanced between analysis cycles with the 15-km nest embedded within the 45-km domain. EAKF analysis ensembles were not re-centered about hybrid analyses. Due to the necessity of 15-km ensembles, this experiment was the most computationally expensive. This experiment's procedure is illustrated in Fig. 3.

2) "Hybrid_DR_1way" : 45-km hybrid analyses were produced as in Hybrid_SR, but ensemble BECs for 15-km hybrid analyses were provided by *45-km* prior ensembles. Thus, the same 45-km ensembles provided BECs for 45-km SR hybrid analyses and 15-km DR hybrid analyses. Since 15-km ensembles were *not* required, the EAKF-WRF ensemble system performed solely 45-km analyses, allowing *removal* of the 15-km nest during the ensemble of WRF model advances between EAKF analyses, enabling considerable savings compared to Hybrid_SR. EAKF analysis ensembles were not re-centered about hybrid analyses. Omission of the re-centering step in Fig. 4 yields this experiment's methodology. Since the 45- and 15-km hybrid analyses were independent and there was no EAKF re-centering, the 45-km analyses and forecasts were identical to the 45-km fields produced in Hybrid_SR.

3) "Hybrid_DR_2way" : Identical to Hybrid_DR_1way, except the 45-km EAKF analysis ensembles were re-centered about *hybrid* analyses. Again, 15-km ensembles were not needed, so the EAKF-WRF ensemble system ran solely at 45-km grid spacing. To perform re-centering, first, the 15-km hybrid analyses were upscaled to 45-km and replaced the 45-km hybrid analyses over the 45-km geographic region co-located with the 15-km grid. Then, each 45-km EAKF analysis ensemble member was re-centered about the 45-km hybrid analysis that contained the upscaled 15-km hybrid analysis information.

Figure 4 exactly depicts this experiment's procedure. The cost of re-centering was nearly negligible, and this experiment had a similar cost as Hybrid_DR_1way.

Comparison of Hybrid_SR with Hybrid_DR_1way cleanly assesses sensitivity to the resolution of the ensemble perturbations, while comparing Hybrid_DR_1way with Hybrid_DR_2way isolates whether re-centering benefits DR hybrid systems. Wang et al. (2013) and Pan et al. (2014) noted little practical difference between SR hybrid systems with and without re-centering steps. Additionally, S13 performed 45-km SR hybrid analyses for this period and domain and noted little sensitivity to whether re-centering occurred, so, here, SR analyses with EAKF re-centering were not performed. We can also compare the 45- and 15-km Hybrid_SR analyses and forecasts to determine the benefit of HR analyses and forecasts.

Results from these experiments are presented in section 7.

5. Observations

As in S13, the WRFDA-hybrid and EAKF systems assimilated different observations, as summarized in Table 2. Observations taken within ± 3-hrs of each analysis time were assimilated and observations were assumed to be valid at the analysis time. A typical distribution of observations available for assimilation at 0000 UTC is shown in Fig. 2. At this time, bogus tropical cyclone (TC) observations produced as in Hsiao et al. (2010) were distributed around typhoon Sinlaku, and a similar spatial distribution of TC bogus observations was used for other TCs. Analyses in both domains only assimilated observations located within their bounds, meaning the 15-km analyses assimilated fewer observations than the 45-km analyses.

All observations were subject to various forms of quality control as in S13. Observations above the model top were excluded from assimilation and at stations where multiple observations were received during the ± 3-hr time-window, only the observation nearest the analysis time was kept. Additionally, "outlier checks" were applied. In the hybrid, an observation was not assimilated if its innovation exceeded $5\sigma_o$, where σ_o is the observation error standard deviation. As in S13, a different outlier check was applied in DART compared to that in the hybrid to account for ensemble spread. Specifically, the EAKF did not assimilate an observation if the ensemble mean innovation was greater than three times the square root of the sum of σ_o^2 and σ_f^2, where σ_f^2 is the ensemble variance of the simulated observation.

6. Results: single-observation experiments

To understand hybrid analysis sensitivity to the resolution of ensemble perturbations, two separate sets of hybrid analyses were performed where solely a single observation was assimilated. The two sets differed by the location of the observation—one was placed within a strong typhoon and the other in nondescript westerly flow. Within each set, SR and DR hybrid analyses were performed that differed by the resolution of the ensemble perturbations. The SR analyses used the 15-km ensemble produced in Hybrid_SR to provide BECs whereas the DR analyses used BECs provided by the 45-km ensemble produced in Hybrid_DR_1way. To ensure that analysis differences were solely attributable to the different ensembles, the background for *all* experiments was the 15-km Hybrid_DR_1way background valid at 0000 UTC 12 September. Further, to maximize potential analysis differences, BECs for all single-observations experiments were provided entirely from the ensemble (no static **B** contribution).

a. Single observation in typhoon core

A single 500 hPa temperature observation placed near the center of typhoon Sinlaku that was 2 K colder than the background (i.e., innovation of -2 K) with an error standard deviation of 1 K was assimilated. There were many differences between the 15-km SR and DR increments. For example, the SR hybrid 500 hPa potential temperature (θ) increments (Fig. 5a) were more negative near the observation than the DR hybrid analysis increments (Fig. 5b), indicating the SR analysis more closely fit the observation. Additionally, while both increments were positive west of the observation, northeast of Taiwan, the DR increments were slightly negative or neutral while the SR increments were positive. Furthermore, the DR analysis had a greater area of negative increments north and east of the observation. Everywhere, the SR increments had more fine-scale detail than the DR increments, and the circulation around Sinlaku was more prominent in the SR increments.

Similarly, near the observation location, the 15-km 500 hPa water vapor mixing ratio increments (Fig. 6a,b) were larger in the SR analysis. While the DR and SR moisture increments were broadly similar west of ~123°E, there were substantial differences near and east of the observation. Specifically, the DR increments were more negative immediately west of the observation, and the SR and DR increments had opposite signs at many locations east of ~125°E. Both increments clearly captured the circulation around the typhoon, illustrating the incorporation of flow-dependent BECs in the hybrid, but the SR increments featured more banded structures and greater detail than the DR increments.

Those disparities between the SR and DR hybrid increments can largely be explained by differences regarding the 45- and 15-km ensembles that provided the BECs for the analyses. Figures 5c,d show the 15- and 45-km ensemble standard deviations of 500 hPa θ at 0000 UTC 12 September overlaid with the ensemble mean 500 hPa height. The 15-km ensemble had a stronger TC than the 45-km ensemble, consistent with the expectation that HR models can better resolve strong TCs than LR models (e.g., Xue et al. 2013). Near the observation, the 15-km ensemble had larger θ spread than the 45-km ensemble, which permitted the SR analysis greater freedom to adjust toward the observation than the DR analysis. The 15-km ensemble θ spread was organized into bands associated with the TC, while the 45-km ensemble θ spread had less-coherent spiraling structures. However, the 45-km 500 hPa ensemble water vapor mixing ratio spread more clearly reflected the TC, but the 15-km spread again had more banding (Fig. 6c,d). Overall, the SR and DR increments usually reflected the ensemble spreads, as the largest increments often corresponded to those regions where ensemble spread was greatest.

b. Single observation in mid-latitude westerly flow

The second set of single-observation experiments assimilated a 500 hPa temperature observation placed at 35°N, 120°E, on the southern periphery of the jet stream. Again, the observation error standard deviation and innovation were 1 K and -2 K, respectively. For this case, the SR and DR 500 hPa potential temperature increments were remarkably similar (Fig. 7a,b), although the SR increments again had finer structures. Furthermore, the 500 hPa 45- and 15-km θ spreads over this region were broadly similar (Fig. 7c,d) and small compared to spread near the TC core. Thus, the increments were smaller than those near the TC core. For other meteorological variables and vertical levels, the DR and SR increments were also very similar (not shown).

c. Discussion

The extent of the differences between the SR and DR hybrid analysis increments depended on the nature of the flow. In benign westerly flow, the 45- and 15-km ensemble spreads were similar and the 15-km SR and DR hybrid increments were nearly identical. However, around typhoon Sinlaku, the DR and SR increments differed substantially, which was related to major differences between the 45- and 15-km ensembles providing the BECs. These single-observation tests suggest that DR and SR hybrid analyses will potentially be most disparate around small-scale features that HR ensembles can better resolve than LR ensembles. In these cases, HR ensembles can be expected to better represent uncertainty, which should lead to more spread compared to LR ensembles. Conversely, in regimes where synoptic-scale flow dominates, HR and LR ensembles are more likely to resolve features similarly, and these single-observation tests suggest that for large-scale patterns, SR and HR hybrid analyses may be quite similar.

The next section objectively verifies analyses and forecasts produced by the SR and DR hybrid systems that assimilated real observations.

7. Results: real data experiments

Model output was compared to TC track forecasts and radiosonde observations. Aspects of the ensemble forecasts were also examined since they are important inputs to the hybrid. The first ~5-days of the simulations were excluded from all verification statistics to allow ample time for the ensemble to “spin-up” from the initial, randomly generated ensemble.

We focus primarily on 15-km WRF forecasts initialized by 15-km hybrid analyses. However, we also show results from 45-km forecasts initialized by 45-km Hybrid_SR analyses, which, given the experimental design, were identical to the 45-km forecasts initialized by 45-km Hybrid_DR_1way analyses. Since the WRF domains were one-way nested, we refer to the 15- and 45-km Hybrid_SR analyses and forecasts as “belonging” to separate, independent systems, even though the 15-km domain was a nest within the 45-km domain and the 15- and 45-km WRF forecasts were produced concurrently (e.g., Fig. 3).

a. Ensemble performance

A high-quality prior ensemble is instrumental to successful hybrid analyses. In a well-calibrated EnKF analysis/forecast system, when compared to observations, the prior ensemble mean root mean square error (RMSE) will equal the prior “total spread,” defined as the square root of the sum of the observation error variance and prior ensemble variance of the simulated observations (Houtekamer et al. 2005). Therefore, the ratio of the prior total spread to the prior ensemble mean RMSE, called the “consistency ratio”

(CR; Dowell and Wicker 2009), should equal 1 in a well-calibrated system. CRs < 1 indicate insufficient ensemble spread.

To enable comparison between the 45- and 15-km prior ensembles, verification occurred against a dataset comprised solely of radiosonde observations assimilated by both the 15- and 45-km EAKFs. The 15- and 45-km ensembles were produced in Hybrid_SR and Hybrid_DR_1way, respectively. The prior RMSE, total spread, and ensemble mean additive bias aggregated between 1800 UTC 8 and 0000 UTC 28 September are shown in Fig. 8 for radiosonde observations. Both ensembles had comparable wind biases and RMSEs (Fig. 8a,b), and the total spread agreed well with the RMSEs at most levels. The 45-km ensemble had poorer temperature biases and RMSEs (Fig. 8c) than the 15-km ensemble below ~850 hPa but performed comparably to or better than the 15-km ensemble at higher levels. For temperature observations, both ensembles had similar total spread that was greater then the corresponding RMSEs between ~400-200 hPa. For specific humidity, at 500, 700, and 850 hPa, both ensembles had comparable RMSEs and dry biases (Fig. 8d). However, at and below 925 hPa, the 15-km ensemble had lower RMSEs than the 45-km ensemble and there were moist biases, although the 15-km ensemble bias was smaller. Throughout the column, the 15-km ensemble had more moisture spread than the 45-km ensemble, but both ensembles had insufficient spread above ~850 hPa.

Both ensembles had CRs near 1 at most levels for wind (Fig. 9a,b), with the 15-km ensemble performing best at and below 700 hPa. For temperature observations (Fig. 9c), at and above 500 hPa, the 45- and 15-km ensembles had comparable CRs, but below 500 hPa, except at 1000 hPa, the 15-km ensemble had CRs closer to 1 than the 45-km ensemble. Similarly, 45-km CRs for specific humidity were closer to 1 than the 15-km ensemble at 1000 hPa (Fig. 9d), but at all other levels, the 15-km CRs for moisture were nearer to 1.

It is also interesting to examine the spatial distribution of the 45- and 15-km ensemble spreads. The average prior ensemble standard deviation of 500 hPa wind speed between 1800 UTC 8 and 0000 UTC 28 September (Fig. 10a,b) was smallest over Eastern China, where observations were plentiful, and portions of the Pacific Ocean where there was little uncertainty about the location of the sub-tropical high-pressure system. The 15-km ensemble had slightly higher spread in most areas. Similar patterns were evident with the mean 500 hPa potential temperature spread (Fig. 10c,d). A local spread maximum was evident in both 500 hPa wind and potential temperature southeast of Taiwan, where three TCs moved, reflecting the uncertainty of TC prediction.

Consistent with Fig. 10, the 15-km ensemble had more spread than the 45-km ensemble throughout the column, as evidenced by the domain average prior ensemble standard deviations between 1800 UTC 8 and 0000 UTC 28 September (Fig. 11). The 45-km statistics were computed solely over the portion of the 45-km domain co-located with the 15-km nest. At all levels for wind and water vapor mixing ratio (Fig. 11a,b,d), the 15-km ensemble had greater spread than the 45-km ensemble, but the 15-km ensemble spread was typically at most 10% greater than the 45-km ensemble spread. The differences between the 15- and 45-km ensemble potential temperature spread (Fig. 11c) were small compared to those for other variables.

Overall, both the 15- and 45-km ensembles were reasonably well calibrated, as CRs were typically within 10% of 1 for most levels and variables. The 15-km ensemble

CRs were usually comparable to or better than the 45-km CRs, and the 15-km ensemble performed notably better than the 45-km ensemble below ~700 hPa, particularly for temperature and moisture. Additionally, the 15-km ensemble had greater spread than the 45-km ensemble, which is sensible, since errors on HR grids grow faster than those on LR grids (e.g., Lorenz 1969). Yet, the differences in spread were usually small, and the next section assesses how these different ensemble spreads impacted the DR and SR hybrid analysis systems.

b. Mean hybrid background and analysis characteristics

The background and analysis fits to observations were also examined. A common observational set consisting of radiosonde observations solely over the 15-km domain was used for verification. The following statistics were aggregated over each hybrid background (6-hr forecasts) and analysis between 1800 UTC 8 and 0000 UTC 28 September (78 total).

All backgrounds had similar average fits to radiosonde wind observations at most levels (Fig. 12a,b). For radiosonde temperature observations (Fig. 12c), the 45-km Hybrid_SR biases were better than the 15-km biases between ~400-200 hPa. The three 15-km analyses had nearly identical mean background fits to temperature and radiosonde specific humidity observations (Fig. 12c,d). However, for specific humidity, the 45-km Hybrid_SR background biases were notably worse than the 15-km biases below 925 hPa.

Figure 13 shows the mean analysis fits to radiosonde observations. On average, the 15-km analyses fit radiosonde wind observations (Fig. 13a,b) more closely than the 45-km SR analysis at most levels, as evidenced by lower 15-km RMSEs and biases closer to zero. There was little difference between the 15-km Hybrid_DR_1way and Hybrid_DR_2way analysis fits, but the 15-km Hybrid_SR RMSEs were smaller than the 15-km Hybrid_DR_1way RMSEs at most levels for zonal wind and below ~500 hPa for meridional wind. This finding is consistent with the 15-km ensemble having slightly more spread than the 45-km ensemble for wind (e.g., Fig. 11). Analysis fits to radiosonde temperature observations (Fig. 13c) were quite similar amongst all analyses, which reflects only minute differences between the 15- and 45-km temperature ensemble spreads. The 15-km analyses more closely fit radiosonde specific humidity observations (Fig. 13d) than the 45-km Hybrid_SR analysis below ~850 hPa. This behavior, and the slightly smaller 15-km Hybrid_SR RMSEs compared to Hybrid_DR_1way below ~850 hPa, is consistent with larger 15-km ensemble spread for specific humidity.

The mean 15-km Hybrid_DR_1way and Hybrid_SR 500 hPa potential temperature (Fig. 14a,b) and 700 hPa water vapor mixing ratio (Fig. 14c,d) analysis increments between 1800 UTC 8 and 0000 UTC 28 September were very similar, although the Hybrid_SR patterns were less smooth. Furthermore, the mean Hybrid_DR_1way and Hybrid_SR 500 and 700 hPa heights (overlaid on Fig. 14) were remarkably similar. The corresponding Hybrid_DR_2way increments and heights were also similar to those of Hybrid_DR_1way and Hybrid_SR (not shown). Despite the 15-km Hybrid_SR analyses sometimes fitting observations slightly closer than the other analyses, the mean increments and prior fits to observations suggest that the three 15-km DA systems performed similarly, on average. We now assess whether these similar analyses translated into comparable forecasts.

c. TC track forecasts

TC forecasts were verified as in S13 using "best track" positions from the Taiwan CWB as "truth." TC positions were diagnosed using a DART forward operator that locates TCs using 800 hPa circulation (e.g., Cavallo et al. 2013). Track error statistics for each storm were computed from multiple WRF forecasts spanning the lifetime of each TC (Table 3). The track of each TC is shown in Fig. 15. Sometimes the experiments failed to predict a TC, and different experiments missed different storms. Performing homogeneous comparisons based solely on storms that all experiments successfully predicted decreased sample sizes. Thus, as in S13, inhomogeneous comparisons amongst the experiments were employed to compare TC track forecasts.

Fig. 16 shows mean absolute track errors and sample sizes at each forecast hour. For Sinlaku (Fig. 16a,b), the 45-km forecast initialized from Hybrid_SR produced the largest track errors and missed the most storms after ~36-hrs, despite having the smallest initial errors. There was little difference between forecasts initialized from the various 15-km hybrid analyses, although Hybrid_DR_2way had the smallest errors after ~42-hrs. For Hagupit (Fig. 16c,d), again, there were few differences between the 15-km forecasts. However, the 15-km forecasts did not improve upon 45-km Hybrid_SR forecasts. This finding is not necessarily surprising, as increased resolution does not always yield better TC forecasts (as discussed in Xue et al. 2013). Hagupit's track was governed by flow around the subtropical high, whose axis firmly extended into eastern China during Hagupit's lifetime. Thus, as a dominant large-scale feature was responsible for Hagupit's movement, the potential benefit of HR was diminished. Track errors for Jangmi (Fig. 16e,f) were qualitatively similar to those for Sinlaku, with the 15-km forecasts improving upon the 45-km Hybrid_SR-initialized forecast. Again, there was little difference between the 15-km forecasts initialized by the various hybrid configurations.

The track errors were also averaged over all three TCs (Fig. 17). All 15-km forecasts improved upon the 45-km Hybrid_SR forecast after ~36-hrs. Track errors from Hybrid_DR_2way were smallest after ~36-hrs, although differences between the 15-km forecasts were small compared to those between the 45- and 15-km forecasts. There was also little difference regarding TC intensity among the 15-km forecasts (not shown), but they were collectively better than the 45-km Hybrid_SR intensity forecasts.

d. Forecast verification versus radiosonde observations

To assess large-scale forecast performance, model output was verified against radiosonde observations at several forecast times. As before, a common observational set consisting of radiosonde observations solely over the 15-km domain was used to verify all experiments. Statistics were aggregated over 78 forecasts initialized every 6-hrs between 1800 UTC 8 and 0000 UTC 28 September.

At 24-hrs, all experiments had similar RMSEs compared to radiosonde wind observations (Fig. 18a,b). The 45-km forecast initialized from Hybrid_SR had slightly worse biases than the 15-km forecasts between ~500-400 hPa but slightly better biases above 250 hPa. There was little difference between the 15-km forecast biases and RMSEs compared to radiosonde temperature and specific humidity observations (Fig. 18c,d). However, the 45-km Hybrid_SR-initialized forecast had the poorest temperature biases and RMSEs below ~500 hPa despite having the best biases above ~250 hPa (Fig. 18c). The 45-km forecast also had the poorest specific humidity biases and RMSEs below 925 hPa (Fig. 18d). Similar patterns were evident at and 36- and 48-hrs (not shown).

At 72-hrs, all experiments usually had similar wind RMSEs and biases (Fig. 19a,b). Temperature and specific humidity biases and RMSEs (Fig. 19c,d) were similar to those at 24-hrs: there was little difference between the 15-km forecasts and the 45-km forecast had higher RMSEs for temperature and specific humidity below 700 hPa but the best temperature bias above ~250 hPa.

8. Summary and conclusion

DR hybrid analysis capability was implemented within the community WRFDA system. The DR hybrid combines observations, a HR background, and a LR ensemble to produce a deterministic HR analysis, permitting considerable computational savings compared to a SR hybrid configuration. DR and SR experiments were performed that produced new hybrid analyses every 6-hrs in a continuously cycling framework over a ~3.5 week period and initialized 72-hr WRF model forecasts. Both the DR and SR hybrid systems ingested flow-dependent BECs provided by a 32-member ensemble that was updated by an EAKF, and different DR configurations examined whether it was preferable to re-center EAKF analysis ensembles about DR hybrid analyses. The DR system combined a 15-km background with a 45-km ensemble, while the SR system combined a background and ensemble with equal, 15-km horizontal grid lengths. SR 45-km analyses and forecasts were also performed.

On average, the 15-km prior ensemble had slightly more spread than the 45-km prior ensemble. This behavior translated into slightly closer 15-km SR analysis fits to radiosonde observations than the 15-km DR hybrid analyses that ingested 45-km ensemble perturbations. However, the mean 15-km SR and DR hybrid analysis increments and prior fits to radiosonde observations were very similar. Overall, 15-km forecasts initialized by 15-km DR and SR analyses were comparable, and re-centering the analysis ensemble about DR hybrid analyses only had a small impact.

These collective results suggest that DR hybrid analyses can initialize similar quality forecasts as SR hybrid analyses. This finding justifies the use of LR ensembles as the source of flow-dependent BECs for HR hybrid analyses and enables substantial computational savings compared to SR systems regarding both disk space and processing. For our experiments, even though 15-km DR hybrid analyses required on average ~28% more iterations to converge than 15-km SR hybrid analyses, the 15-km DR analyses nonetheless finished ~3 times faster than the 15-km SR analyses, primarily because the DR hybrid had fewer extended control variables. Additionally, during the ensemble of WRF model advances between EAKF analyses, the DR configuration realized a three-fold savings compared to the 15-km SR hybrid, since the 15-km nest was removed in the DR configuration for each ensemble member because a 15-km EAKF analysis was not required (e.g., Fig. 4). Moreover, the 15-km SR hybrid required ~4 times more disk space than the 15-km DR hybrid, as the 15-km SR hybrid required storage of 15-km perturbations, whereas the 15-km DR hybrid solely needed 45-km perturbations. These savings could be utilized for many purposes, including increasing the ensemble size, which may benefit hybrid analyses.

Here, the HR horizontal grid spacing was 3 times finer than the LR horizontal grid length. As the ratio of LR to HR horizontal grid spacing increases, so do the computational savings, but a larger grid ratio may translate into greater differences between SR and DR hybrid analysis/forecast systems than documented here. Additionally, an important question regards the utility of DR hybrid systems at increased resolution, particularly when the background is at sufficiently fine resolution that convective parameterization (CP) can be removed but the ensemble resolution is coarse enough that CP is required. In such a configuration, the CP scheme may engender very different bias characteristics (e.g., Romine et al. 2013) in the prior ensemble compared to those of the convection-allowing background. It is unclear how much of an impact this disparity may have, but this topic demands investigation as NWP models continue their progression toward higher resolution.

Acknowledgements

The Taiwan Central Weather Bureau (CWB) partially funded this work. NCAR is sponsored by the National Science Foundation.

References

Anderson, J. L., 2001: An ensemble adjustment Kalman filter for data assimilation. *Mon. Wea. Rev.*, **129,** 2884–2903.

Anderson, J. L., 2003: A Local Least Squares Framework for Ensemble Filtering. *Mon. Wea. Rev.*, **131,** 634–642.

Anderson, J. L., 2009: Spatially and temporally varying adaptive covariance inflation for ensemble filters. *Tellus*, **61A**, 72–83.

Anderson, J. L., T. Hoar, K. Raeder, H. Liu, N. Collins, R. Torn, and A. Arellano, 2009: The Data Assimilation Research Testbed: A community facility. *Bull. Amer. Meteor. Soc.*, **90,** 1283–1296.

Barker, D. M., 2005: Southern high-latitude ensemble data assimilation in the Antarctic Mesoscale Prediction System. *Mon. Wea. Rev.*, **133**, 3431–3449.

Barker, D. M., W. Huang, Y-R. Guo, A. Bourgeois, and X. N. Xio, 2004: A three-dimensional variational data assimilation system for MM5: Implementation and initial results. *Mon. Wea. Rev.*, **132,** 897–914.

Barker, D., and Coauthors, 2012: The Weather Research and Forecasting Model's Community Variational/Ensemble Data Assimilation System: WRFDA. *Bull. Amer. Meteor. Soc.*, **93**, 831–843.

Berner, J., G. J. Shutts, M. Leutbecher, and T. N. Palmer, 2009: A spectral stochastic kinetic energy backscatter scheme and its impact on flow-dependent predictability in the ECMWF ensemble prediction system. *J. Atmos. Sci.*, **66**, 603–626.

Buehner, M., 2005: Ensemble-derived stationary and flow-dependent background error covariances: Evaluation in a quasi-operational NWP setting. *Quart. J. Roy. Meteor. Soc.*, **131,** 1013–1043.

Buehner, M., P. L. Houtekamer, C. Charette, H. L. Mitchell, and B. He, 2010: Intercomparison of variational data assimilation and the ensemble Kalman filter for global deterministic NWP. Part II: One-month experiments with real observations. *Mon. Wea. Rev.*, **138**, 1567–1586.

Burgers, G., P. J. van Leeuwen, and G. Evensen, 1998: Analysis scheme in the ensemble Kalman filter. *Mon. Wea. Rev*, **126,** 1719–1724.

Campbell, W. F., C. H. Bishop, and D. Hodyss, 2010: Vertical covariance localization for satellite radiances in ensemble Kalman filters. *Mon. Wea. Rev.*, **138,** 282–290.

Cavallo, S. M., R. D. Torn, C. Snyder, C. Davis, W. Wang, and J. Done, 2013: Evaluation of the Advanced Hurricane WRF data assimilation system for the 2009 Atlantic hurricane season. *Mon. Wea. Rev.*, **141**, 523–541.

Chen, F., and J. Dudhia, 2001: Coupling an advanced land-surface/ hydrology model with the Penn State/NCAR MM5 modeling system. Part I: Model description and implementation. *Mon. Wea. Rev.*, **129,** 569–585.

Chou M.-D., and M. J. Suarez, 1994: An efficient thermal infrared radiation parameterization for use in general circulation models. NASA Tech. Memo. 104606, 3, 85pp.

Clayton A. M., Lorenc A. C. and Barker D. M., 2012: Operational implementation of a hybrid ensemble/4D-Var global data assimilation system at the Met Office. *Q. J. R. Meteorol. Soc.* doi:10.1002/qj.2054.

Courtier, P., J.-N. Thépaut, and A. Hollingsworth, 1994: A strategy for operational implementation of 4D-Var, using an incremental approach. *Quart. J. Roy. Meteor. Soc.*, **120**, 1367–1387.

Dowell, D. C., and L. J. Wicker, 2009: Additive noise for storm-scale ensemble data assimilation. *J. Atmos. Oceanic Technol.*, **26**, 911–927.

Evensen, G., 1994: Sequential data assimilation with a nonlinear quasi-geostrophic model using Monte Carlo methods to forecast error statistics. *J. Geophys. Res.*, **99,** 10143–10162.

Gao, J., and M. Xue, 2008: An efficient dual-resolution approach for ensemble data assimilation and tests with assimilated Doppler radar data. *Mon. Wea. Rev.*, **136**, 945–963.

Gao, J., M. Xue, and D. J. Stensrud, 2013: The Development of a Hybrid EnKF-3DVAR Algorithm for Storm-Scale Data Assimilation. *Advances in Meteorology*, **2013**, Article ID 512656, doi:10.1155/2013/512656.

Ha, S.-Y., and C. Snyder, 2014: Influence of surface observations in mesoscale data assimilation using an ensemble Kalman filter. *Mon. Wea. Rev.*, doi:10.1175/MWR-D-13-00108.1, In press.

Hamill, T. M., and C. Snyder, 2000: A hybrid ensemble Kalman filter–3D variational analysis scheme. *Mon. Wea. Rev.*, **128**, 2905–2919.

Hamill, T. M., J. S. Whitaker, D. T. Kleist, M. Fiorino, and S. G. Benjamin, 2011: Predictions of 2010's tropical cyclones using the GFS and ensemble-based data assimilation methods. *Mon. Wea. Rev.*, **139**, 3243–3247.

Hong, S-Y., Y. Noh, and J. Dudhia, 2006: A new vertical diffusion package with an explicit treatment of entrainment processes. *Mon. Wea. Rev.*, **134,** 2318–2341.

Houtekamer, P. L., and H. L. Mitchell, 1998: Data assimilation using an ensemble Kalman filter technique. *Mon. Wea. Rev*, **126,** 796–811.

Houtekamer, P. L., H. L. Mitchell, G. Pellerin, M. Buehner, M. Charron, L. Spacek, and B. Hansen, 2005: Atmospheric data assimilation with an ensemble Kalman filter: Results with real observations. *Mon. Wea. Rev.*, **133,** 604–620.

Hsiao, L. F., C. S. Liou, T. C. Yeh, Y. R. Guo, D. S. Chen, K. N. Huang, C. T. Terng, and J. H. Chen, 2010: A vortex relocation scheme for tropical cyclone initialization in Advanced Research WRF. *Mon. Wea. Rev.*, **138**, 3298–3315.

Huang, X.-Y., and P. Lynch, 1993: Diabatic digital filter initialization: Application to the HIRLAM model. *Mon. Wea. Rev.*, **121**, 589–603.

Kain, J. S., and J. M. Fritsch, 1990: A one-dimensional entraining/detraining plume model and its application in convective parameterization. *J. Atmos. Sci.* **47**, 2784–2802.

Kain, J. S., and J. M. Fritsch, 1993: Convective parameterization for mesoscale models: The Kain–Fritsch scheme. *The Representation of Cumulus Convection in Numerical Models, Meteor. Monogr.,* No. 24, Amer. Meteor. Soc., 165–170.

Kain, J. S., 2004: The Kain–Fritsch convective parameterization: An update. *J. Appl. Meteor.*, **43,** 170–181.

Kuhl, D. D., T. E. Rosmond, C. H. Bishop, J. McLay, and N. L. Baker, 2013: Comparison of hybrid ensemble/4DVar and 4DVar within the NAVDAS-AR data assimilation framework. *Mon. Wea. Rev.*, **141**, 2740–2758.

Li, Y., X. Wang, and M. Xue, 2012: Assimilation of radar radial velocity data with the WRF ensemble-3DVAR hybrid system for the prediction of hurricane Ike (2008). *Mon. Wea. Rev.*, **140**, 3507–3524.

Lorenc, A. C., 2003: The potential of the ensemble Kalman filter for NWP—A comparison with 4D-VAR. *Quart. J. Roy. Meteor. Soc.*, **129**, 3183–3203.Lorenz, E. N., 1969: The predictability of a flow which possesses many scales of motion. *Tellus*, **21**, 289–307.

Lynch, P., and X.-Y. Huang, 1992: Initialization of the HIRLAM model using a digital filter. *Mon. Wea. Rev.*, **120**, 1019–1034.

Lynch, P., 1997: The Dolph–Chebyshev window: A simple optimal filter. *Mon. Wea. Rev.*, **125**, 655–660.

Ma, L.-M. and Z.-M. Tan, 2009: Improving the behavior of the cumulus parameterization for tropical cyclone prediction: convection trigger *Atmos. Res.*, **92** (2) 190–211.

Mlawer, E. J., S. J. Taubman, P. D. Brown, M. J. Iacono, and S. A. Clough, 1997: Radiative transfer for inhomogeneous atmosphere: RRTM, a validated correlated-*k* model for the long-wave. *J. Geophys. Res.*, **102,** 16663–16682.

Pan, Y., K. Zhu, M. Xue, X. Wang, J. S. Whitaker, S. G. Benjamin, S. S. Weygandt, and M. Hu, 2014: A regional GSI-based EnKF-variational hybrid data assimilation system for the Rapid Refresh configuration: Results with a single, reduced resolution. *Mon. Wea. Rev.*, Conditionally accepted.

Parrish, D. F., and J. C. Derber, 1992: The National Meteorological Center's spectral statistical interpolation analysis system. *Mon. Wea. Rev.*, **120,** 1747–1763.

Rainwater, S., and B. Hunt, 2013: Mixed resolution ensemble data assimilation. *Mon.*

Wea. Rev., **141**, 3007–3021.

Romine, G., C. S. Schwartz, C. Snyder, J. Anderson, and M. Weisman, 2013: Model bias in a continuously cycled assimilation system and its influence on convection-permitting forecasts. *Mon. Wea. Rev.*, **141**, 1263–1284.

Schwartz, C. S., and Z. Liu, 2014: Convection-permitting forecasts initialized with continuously cycling limited-area 3DVAR, ensemble Kalman filter, and "hybrid" variational–ensemble data assimilation systems. *Mon. Wea. Rev.*, **142**, 716–738.

Schwartz, C. S., Z. Liu, X.-Y. Huang, Y.-H. Kuo, and C.-T. Fong, 2013: Comparing limited-area 3DVAR and hybrid variational-ensemble data assimilation methods for typhoon track forecasts: Sensitivity to outer loops and vortex relocation. *Mon. Wea. Rev.*, **141**, 4350–4372.

Shutts, G., 2005: A kinetic energy backscatter algorithm for use in ensemble prediction systems. *Quart. J. Roy. Meteor. Soc.*, **131**, 3079–3102.

Skamarock, W. C., J. B. Klemp, J. Dudhia, D. O. Gill, D. M. Barker, M. G. Duda, X-Y. Huang, W. Wang, and J. G. Powers, 2008: A description of the Advanced Research WRF version 3. NCAR Tech Note NCAR/TN-475+STR, 113 pp. [Available from UCAR Communications, P. O. Box 3000, Boulder, CO 80307.]

Tao, W.-K., and J. Simpson, 1993: The Goddard cumulus ensemble model. Part I: Model description. *Terr. Atmos. Oceanic Sci.,* **4,** 35–72.

Tao, W.-K., J. Simpson, D. Baker, S. Braun, M.-D. Chou, B. Ferrier, D. Johnson, A. Khain, S. Lang, B. Lynn, C.-L. Shie, D. Starr, C.-H. Sui, Y. Wang, and P. Wetzel, 2003: Microphysics, radiation and surface processes in the Goddard Cumulus Ensemble (GCE) model. *Meteor. and Atmos. Phys*., **82,** 97–137.

Torn, R. D., G. J. Hakim, and C. Snyder, 2006: Boundary conditions for limited-area ensemble Kalman filters. *Mon. Wea. Rev.*, **134,** 2490–2502.

Wang, X., 2010: Incorporating ensemble covariance in the gridpoint statistical interpolation (GSI) variational minimization: A mathematical framework. *Mon. Wea. Rev.*, **138**, 2990–2995.

Wang, X., 2011: Application of the WRF Hybrid ETKF–3DVAR data assimilation system for hurricane track forecasts. *Wea. Forecasting*, **26**, 868–884.

Wang, X., T. M. Hamill, J. S. Whitaker, and C. H. Bishop, 2007a: A comparison of hybrid ensemble transform Kalman filter–OI and ensemble square-root filter analysis schemes. *Mon. Wea. Rev.*, **135**, 1055–1076.

Wang, X., C. Snyder, and T. M. Hamill, 2007b: On the theoretical equivalence of differently proposed ensemble/3D–Var hybrid analysis schemes. *Mon. Wea. Rev.*, **135**, 222–227.

Wang, X., D. Barker, C. Snyder, and T. M. Hamill, 2008a: A hybrid ETKF–3DVAR data assimilation scheme for the WRF model. Part I: Observing system simulation experiment. *Mon. Wea. Rev.*, **136**, 5116–5131.

Wang, X., D. Barker, C. Snyder, and T. M. Hamill, 2008b: A hybrid ETKF–3DVAR data assimilation scheme for the WRF model. Part II: Real observation experiments. *Mon. Wea. Rev.*, **136**, 5132–5147.

Wang, X., D. F. Parrish, D. T. Kleist, and J. S. Whitaker, 2013: GSI 3DVAR-based ensemble-variational hybrid data assimilation for NCEP Global Forecast System: Single-resolution experiments. *Mon. Wea. Rev.*, **141**, 4098–4117.

Whitaker, J. S., T. M. Hamill, X. Wei, Y. Song, and Z. Toth, 2008: Ensemble data assimilation with the NCEP Global Forecast System. *Mon. Wea. Rev.*, **136**, 463–482.

Xue, M., J. Schleif, F. Kong, K. W. Thomas, Y. Wang, and K. Zhu, 2013: Track and intensity forecasting of hurricanes: Impact of convection-permitting resolution and global ensemble Kalman filter analysis on 2010 Atlantic season forecasts. *Wea. Forecasting*, **28**, 1366–1384.

Zhang, F., M. Zhang, and J. A. Hansen, 2009: Coupling ensemble Kalman filter with four-dimensional variational data assimilation. *Adv. Atmos. Sci.*, **26**, 1–8.

Zhang, F., M. Zhang, and J. Poterjoy, 2013: E3DVar: Coupling an ensemble Kalman filter with three-dimensional variational data assimilation in a limited-area weather prediction model and comparison to E4DVar. *Mon. Wea. Rev.*, **141**, 900–917.

Zhang, M., and F. Zhang, 2012: E4DVar: Coupling an ensemble Kalman filter with four-dimensional variational data assimilation in a limited-area weather prediction model. *Mon. Wea. Rev.*, **140**, 587–600.

TABLES

Physical parameterization	WRF option	References
Microphysics	Goddard	Tao and Simpson 1993; Tao et al. 2003
Longwave radiation	Rapid Radiative Transfer Model	Mlawer et al. 1997
Shortwave radiation	Goddard	Chou and Suarez 1994
Planetary boundary layer	Yonsei University	Hong et al. 2006
Land surface model	Noah	Chen and Dudhia 2001
Cumulus parameterization	Kain-Fritsch with modified trigger function	Kain and Fritsch 1990, 1993; Kain 2004; Ma and Tan 2009

Table 1. Physical parameterizations used in both WRF domains.

Observing platform	Observation type Assimilated in WRFDA-hybrid	Observation type Assimilated in DART	Notes
Radiosonde	Surface pressure Temperature Specific humidity Wind	Surface pressure Temperature Specific humidity Wind	
Aircraft	Temperature Wind	Temperature Wind	DART: superobbed in 100 km x 100 km x 25 hPa boxes
Global positioning system radio occultation (GPSRO)	Refractivity	Refractivity	
Satellite-tracked winds	Wind	Wind	DART: Assimilated over water only DART: Superobbed in 100 km x 100 km x 25 hPa boxes
QuikScat	Wind	Not assimilated	WRFDA-hybrid: Assimilated over water only
Ship and buoy	Surface pressure Temperature Specific humidity Wind	Surface pressure Temperature Specific humidity Wind	
SYNOP and METAR	Surface pressure Temperature Specific humidity Wind	Surface pressure	
Bogus	Temperature Specific humidity Wind	Relative humidity Wind	DART: only assimilated at 700 hPa

Table 2. Assimilated meteorological observations in the WRFDA-hybrid and DART systems. See Schwartz et al. (2013) for more information.

Storm	Beginning time	Ending time
Sinlaku	1800 UTC 8 September	0600 UTC 20 September
Hagupit	1200 UTC 19 September	1800 UTC 24 September
Jangmi	1200 UTC 24 September	0000 UTC 1 October

Table 3. The beginning and ending times that were verified for each TC.

FIGURE CAPTIONS

Fig. 1. Two hypothetical examples of valid nested WRF domains.

Fig. 2. Computational domain overlaid with observations available for assimilation during the 0000 UTC 13 September analysis. The inner box represents the bounds of the 15-km domain, which is nested within the 45-km domain.

Fig. 3. Flow-chart describing a cycling EAKF and single-resolution hybrid system where separate, independent 45- and 15-km EAKF and hybrid analyses are performed.

Fig. 4. Flow-chart describing a cycling EAKF and dual-resolution hybrid system where the EAKF analysis ensemble is re-centered about the hybrid analysis.

Fig. 5. The 15-km 500 hPa potential temperature analysis increments at 0000 UTC 12 September for (a) SR (b) DR analyses that assimilated a single observation at the location indicated by asterisks. The background 500 hPa height (m; contoured every 40 m) is overlaid. (c,d) The 500 hPa potential temperature (c) 15-km and (d) 45-km prior ensemble standard deviations at 0000 UTC 12 September overlaid with the ensemble mean prior 500 hPa height. The asterisks in (c) and (d) mark the location of the single assimilated observation that produced increments in (a) and (b). Note that the height fields in (a-b) differ from those in (c-d) because the heights in (a-b) were from the deterministic background while those in (c-d) were from the ensemble mean.

Fig. 6. As in Fig. 5 but for 500 hPa water vapor mixing ratio.

Fig. 7. As in Fig. 5, but increments were engendered by assimilation of a different observation, whose location is indicated by the asterisks.

Fig. 8. Average prior total spread, ensemble mean RMSE, and ensemble mean bias of radiosonde (a) zonal wind (m/s), (b) meridional wind (m/s), (c) temperature (K), and (d) specific humidity (g/kg) between 1800 UTC 8 and 0000 UTC 28 September. The sample size at each pressure level is shown at the right of each panel.

Fig. 9. As in Fig. 8 except for consistency ratios.

Fig. 10. Average prior ensemble standard deviation (spread) of 500 hPa (a,b) wind speed (m/s) and (c,d) potential temperature (K) between 1800 UTC 8 and 0000 UTC 28 September for the (a,c) 45- and (b,d) 15-km ensembles.

Fig. 11. Domain average prior ensemble standard deviations between 1800 UTC 8 and 0000 UTC 28 September for (a) zonal wind (m/s), (b) meridional wind (m/s), (c) potential temperature (K), and (d) water vapor mixing ratio (g/kg). The approximate pressures (hPa) of selected model levels are shown on the right axes of (b) and (d). The 45-km statistics were computed solely over the portion of the 45-km domain co-located with the 15-km domain.

Fig. 12. RMSE (solid lines) and bias (dashed lines) for verification versus radiosonde (a) zonal wind (m/s), (b) meridional wind (m/s), (c) temperature (K), and (d) specific humidity (g/kg) observations averaged over all backgrounds (6-hr forecasts) between 1800 UTC 8 and 0000 UTC 28 September. The sample size at each level is denoted to the right of each panel.

Fig. 13. As in Fig. 12 but for the mean analysis fits to observations.

Fig. 14. 15-km 500 hPa potential temperature analysis increments (K), wind vector increments (arrows), and mean background 500 hPa height (m) averaged between 1800 UTC 8 and 0000 UTC 28 September for (a) Hybrid_SR and (b) Hybrid_DR_1way. (c,d) As in (a,b) except for 700 hPa water vapor mixing ratio increments (g/kg), wind vector increments, and mean background height. Hatching in (c) and (d) indicates those areas where the 700 hPa surface was underground. Heights are contoured every 20 meters in (a,b) and every 10 meters in (c,d).

Fig. 15. (a) Best track positions of tropical cyclones Sinlaku, Hagupit, and Jangmi. Locations are plotted every 6-hrs. See Table 3 for the starting and ending times of each storm.

Fig. 16. Mean 0-72-hr absolute track errors (km) and sample sizes for (a,b) Sinlaku, (c,d) Hagupit, and (e,f) Jangmi.

Fig. 17. As in Fig. 16 but track errors averaged over the three TCs and the total sample size.

Fig 18. Average RMSE (solid lines) and bias (dashed lines) for verification of 24-hr forecasts versus radiosonde (a) zonal wind (m/s), (b) meridional wind (m/s), (c) temperature (K), and (d) specific humidity observations averaged over all 24-hr forecasts. The sample size at each level is denoted to the right of each panel.

Fig. 19. As in Fig. 18 but for 72-hr forecasts.

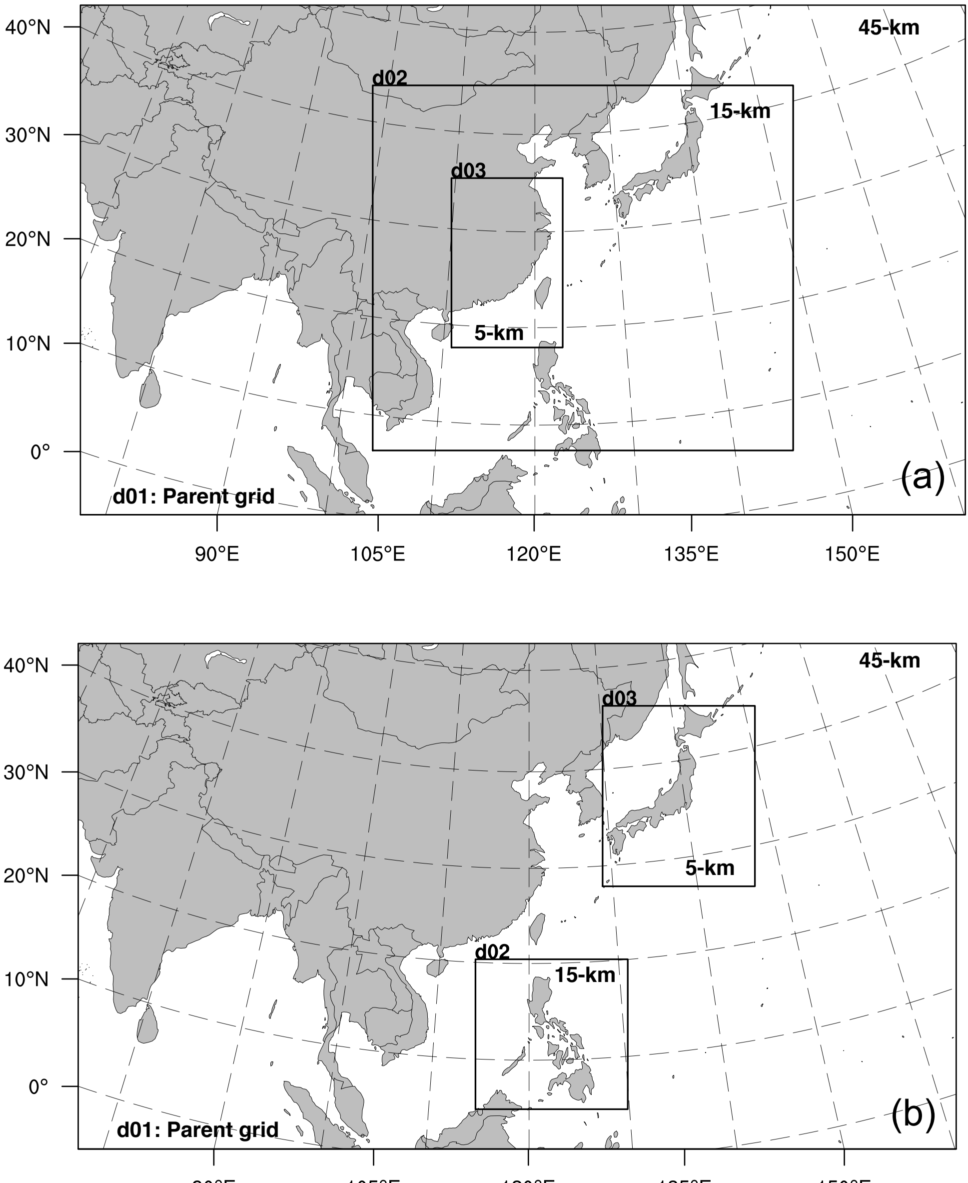

Fig. 1. Two hypothetical examples of valid nested WRF domains.

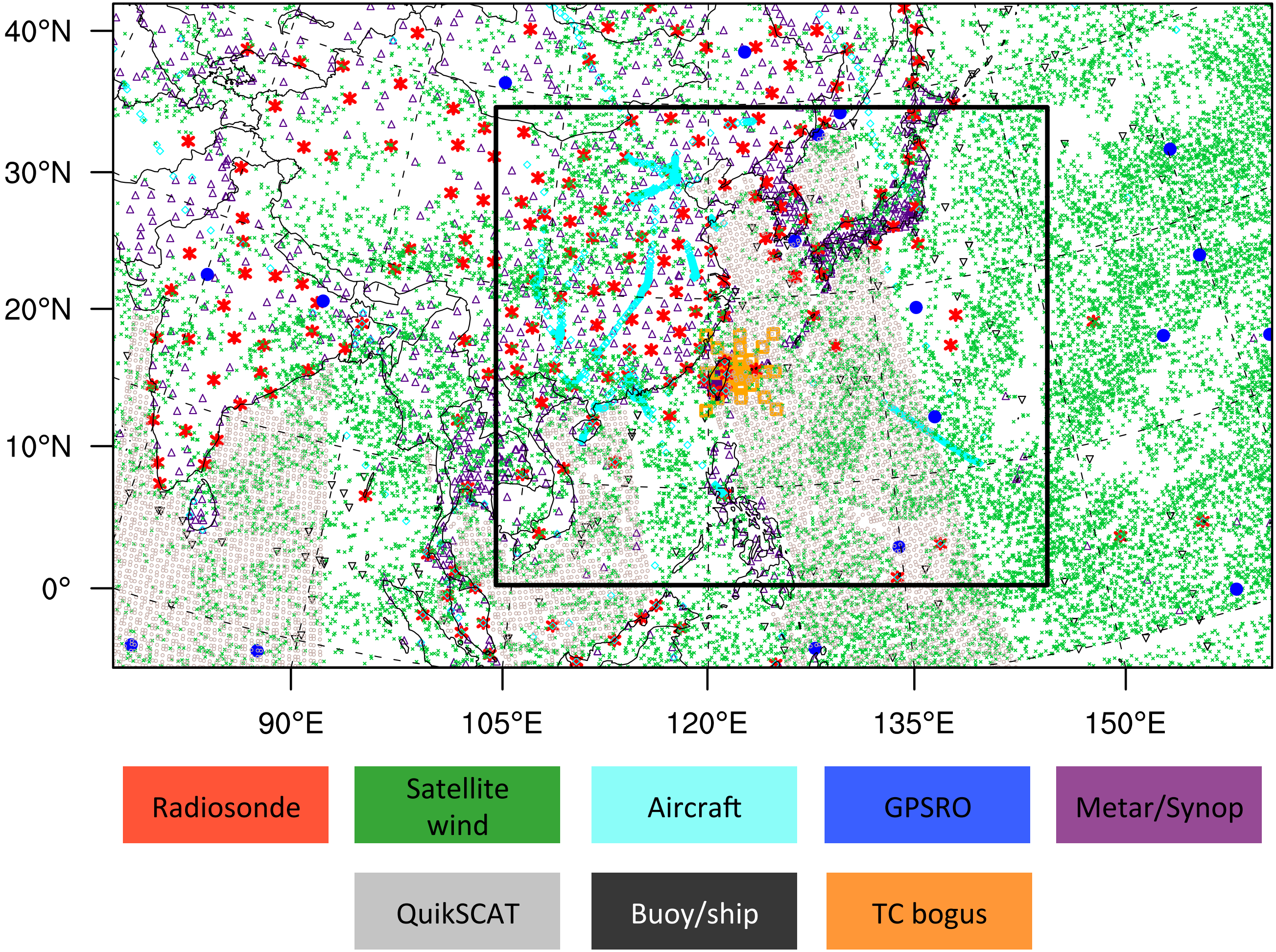

Fig. 2. Computational domain overlaid with observations available for assimilation during the 0000 UTC 13 September analysis. The inner box represents the bounds of the 15-km domain, which is nested within the 45-km domain.

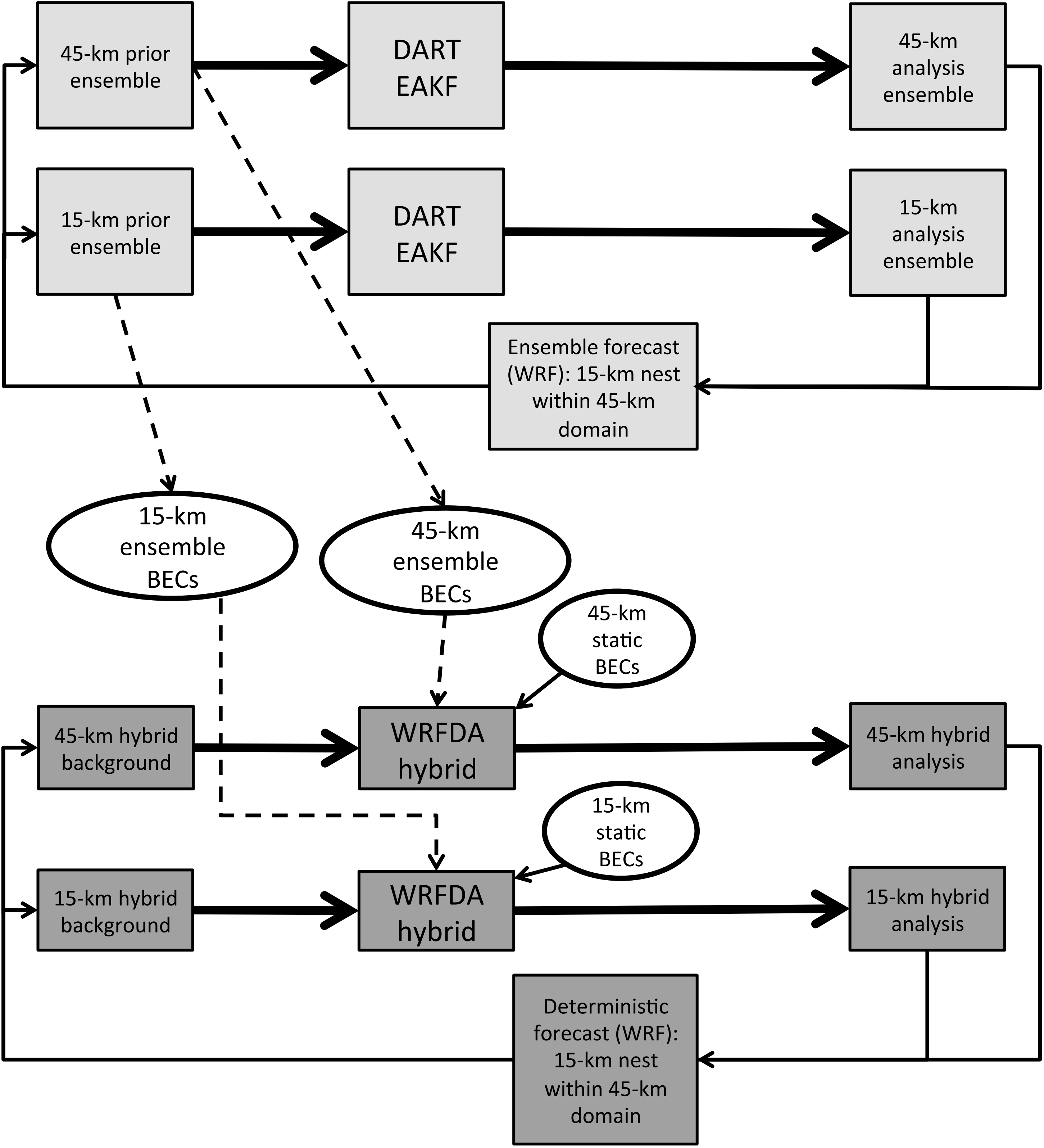

Fig. 3. Flow-chart describing a cycling EAKF and single-resolution hybrid system where separate, independent 45- and 15-km EAKF and hybrid analyses are performed.

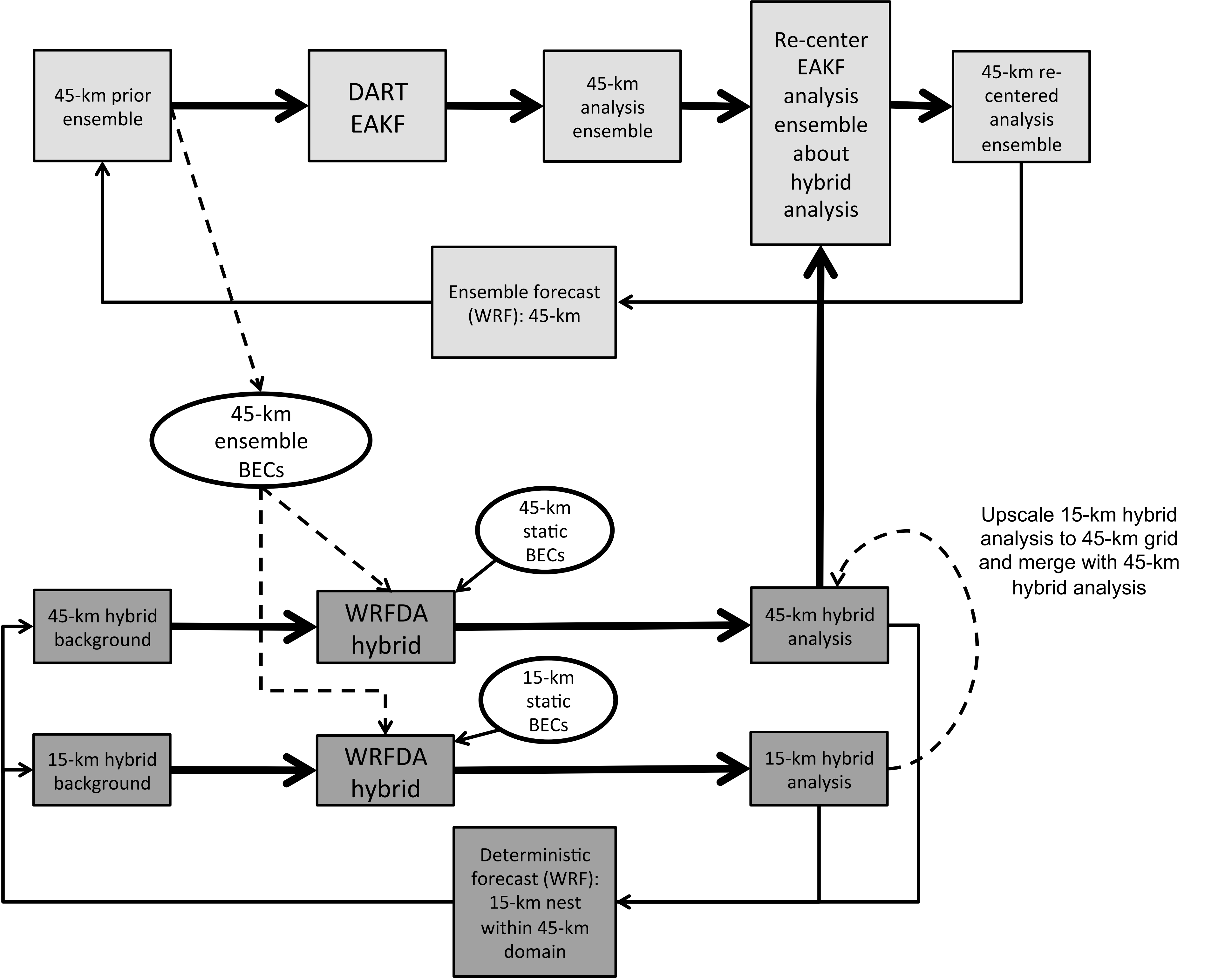

Fig. 4. Flow-chart describing a cycling EAKF and dual-resolution hybrid system where the EAKF analysis ensemble is re-centered about the hybrid analysis.

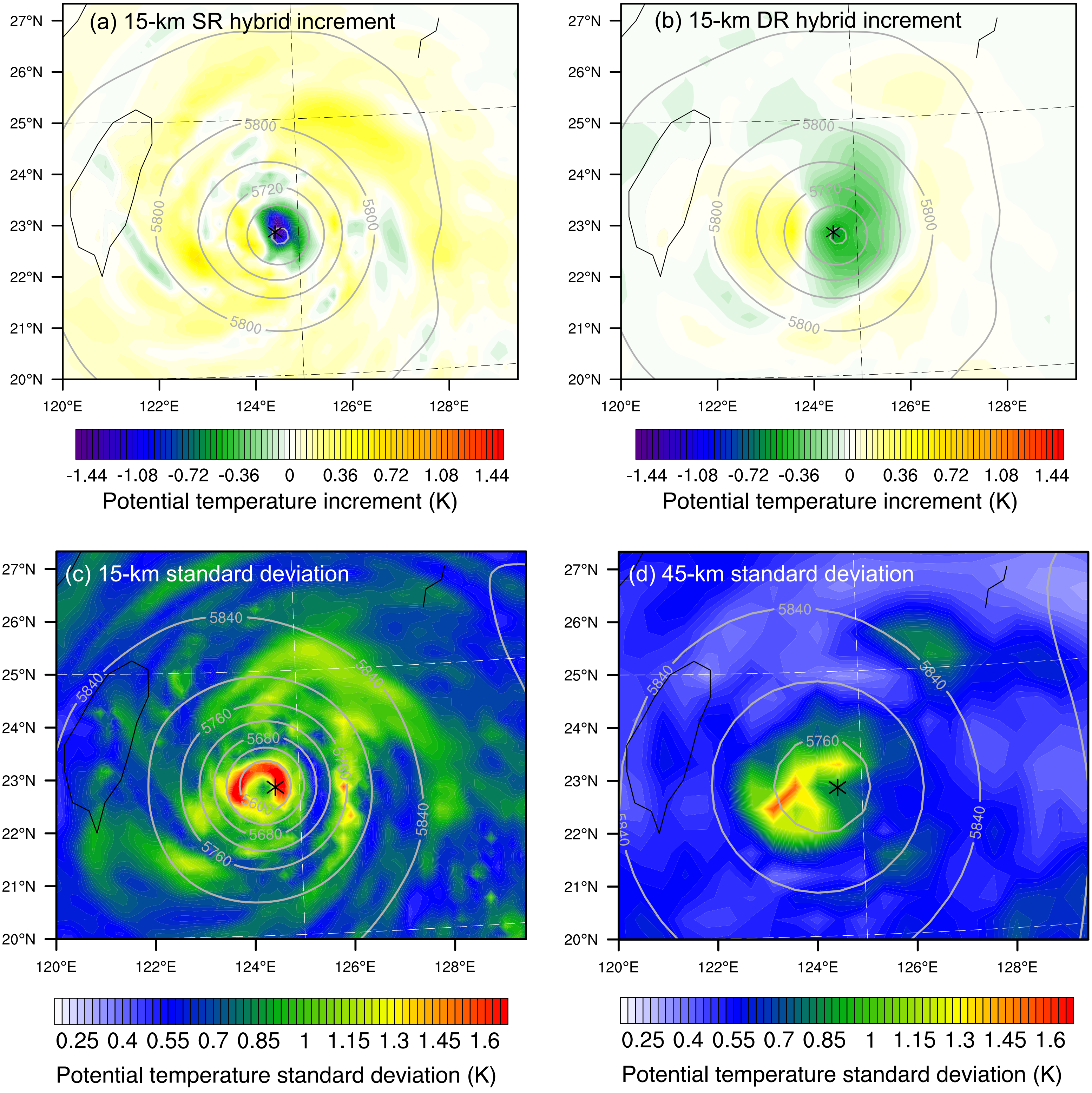

Fig. 5. The 15-km 500 hPa potential temperature analysis increments at 0000 UTC 12 September for (a) SR (b) DR analyses that assimilated a single observation at the location indicated by asterisks. The background 500 hPa height (m; contoured every 40 m) is overlaid. (c,d) The 500 hPa potential temperature (c) 15-km and (d) 45-km prior ensemble standard deviations at 0000 UTC 12 September overlaid with the ensemble mean prior 500 hPa height. The asterisks in (c) and (d) mark the location of the single assimilated observation that produced increments in (a) and (b). Note that the height fields in (a-b) differ from those in (c-d) because the heights in (a-b) were from the deterministic background while those in (c-d) were from the ensemble mean.

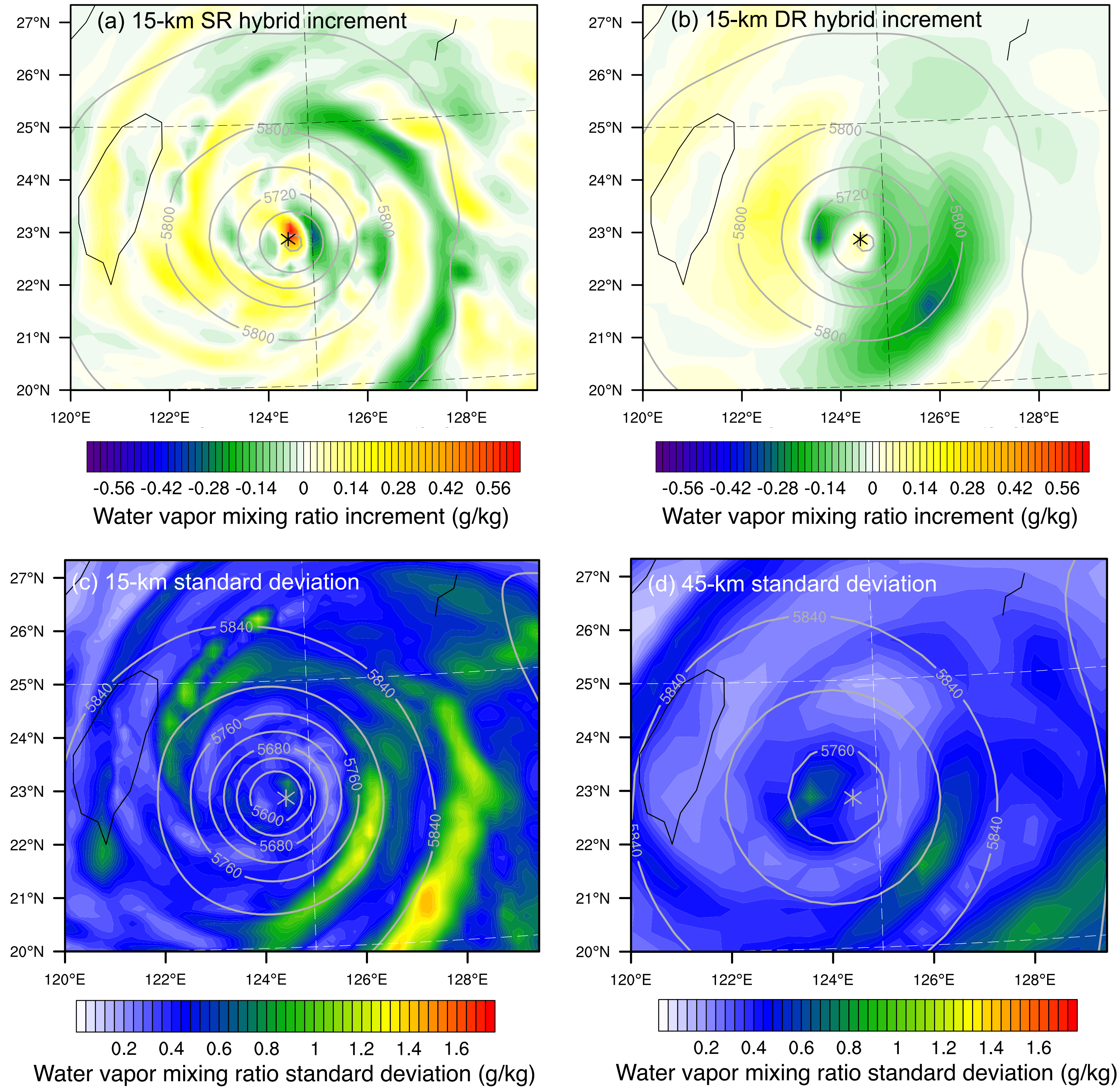

Fig. 6. As in Fig. 5 but for 500 hPa water vapor mixing ratio.

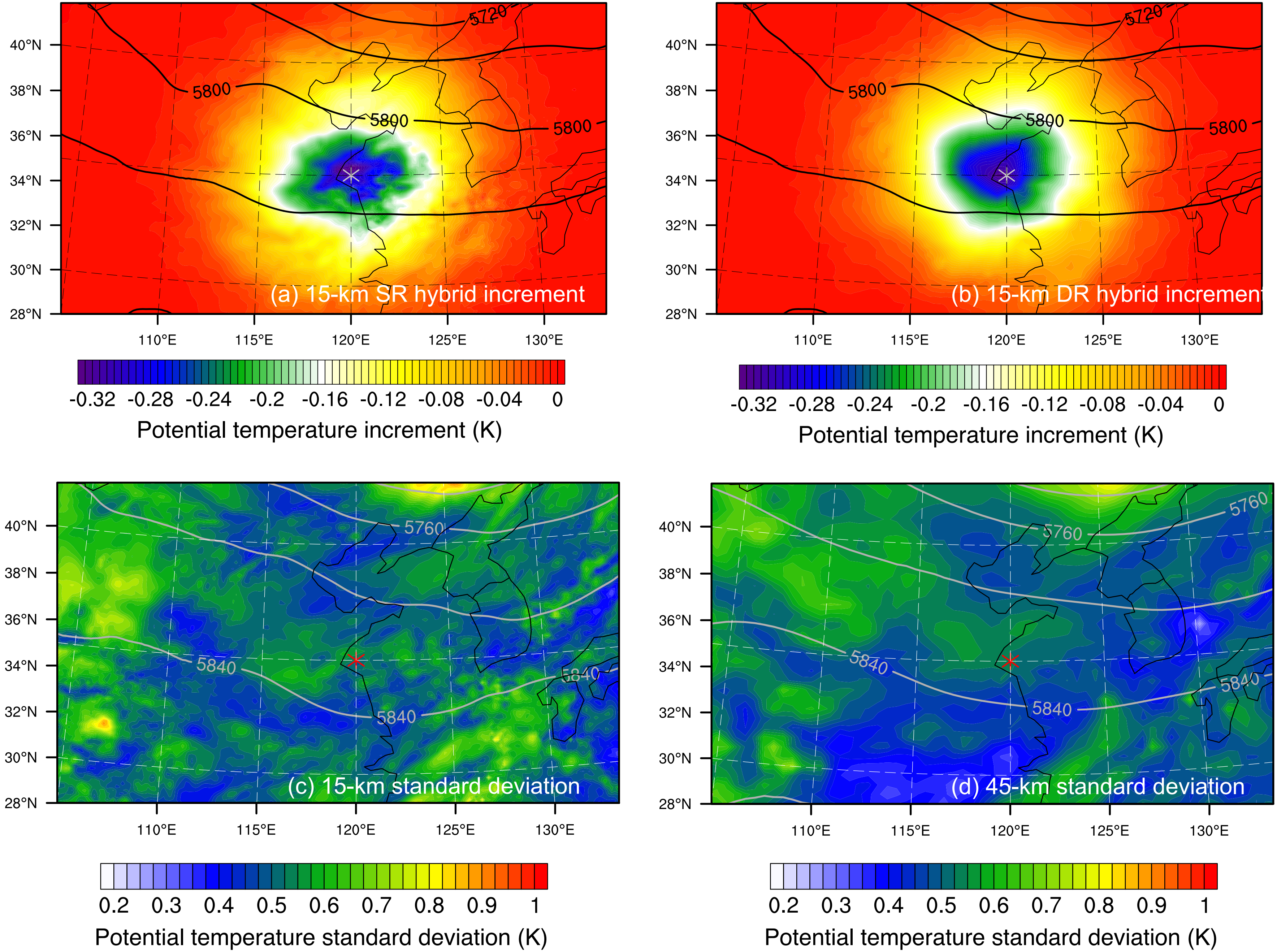

Fig. 7. As in Fig. 5, but increments were engendered by assimilation of a different observation, whose location is indicated by the asterisks.

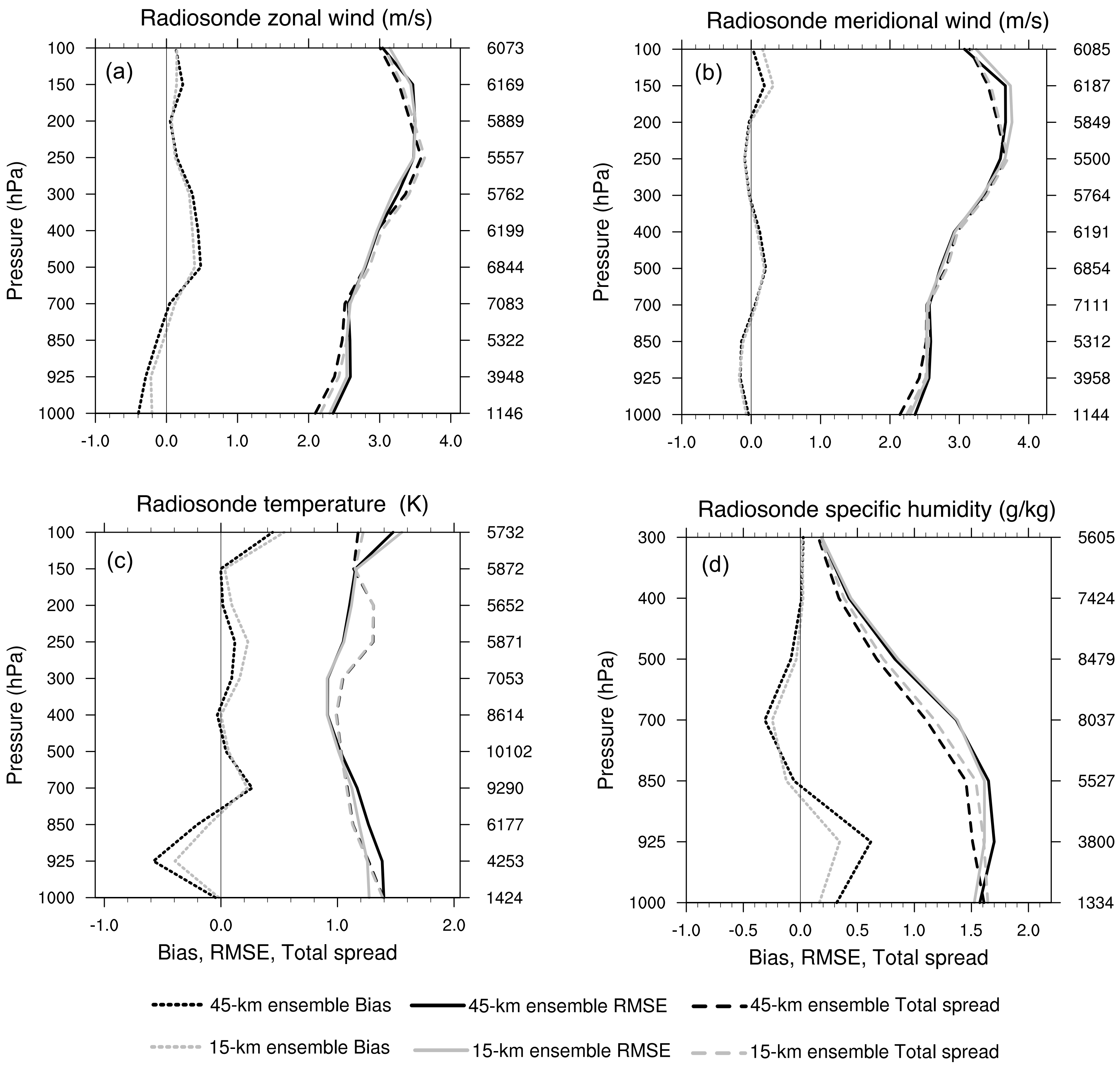

Fig. 8. Average prior total spread, ensemble mean RMSE, and ensemble mean bias of radiosonde (a) zonal wind (m/s), (b) meridional wind (m/s), (c) temperature (K), and (d) specific humidity (g/kg) between 1800 UTC 8 and 0000 UTC 28 September. The sample size at each pressure level is shown at the right of each panel.

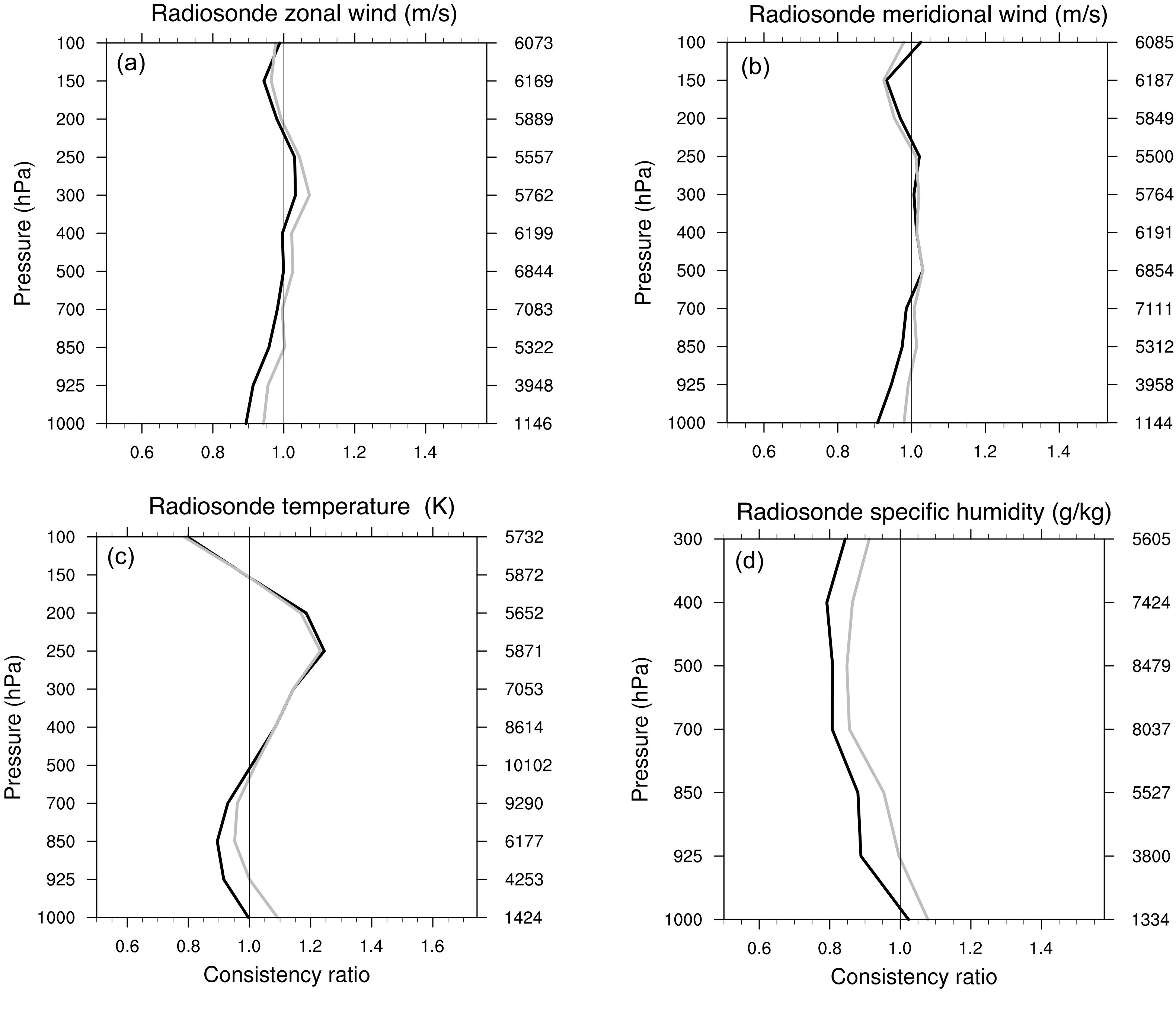

Fig. 9. As in Fig. 8 except for consistency ratios.

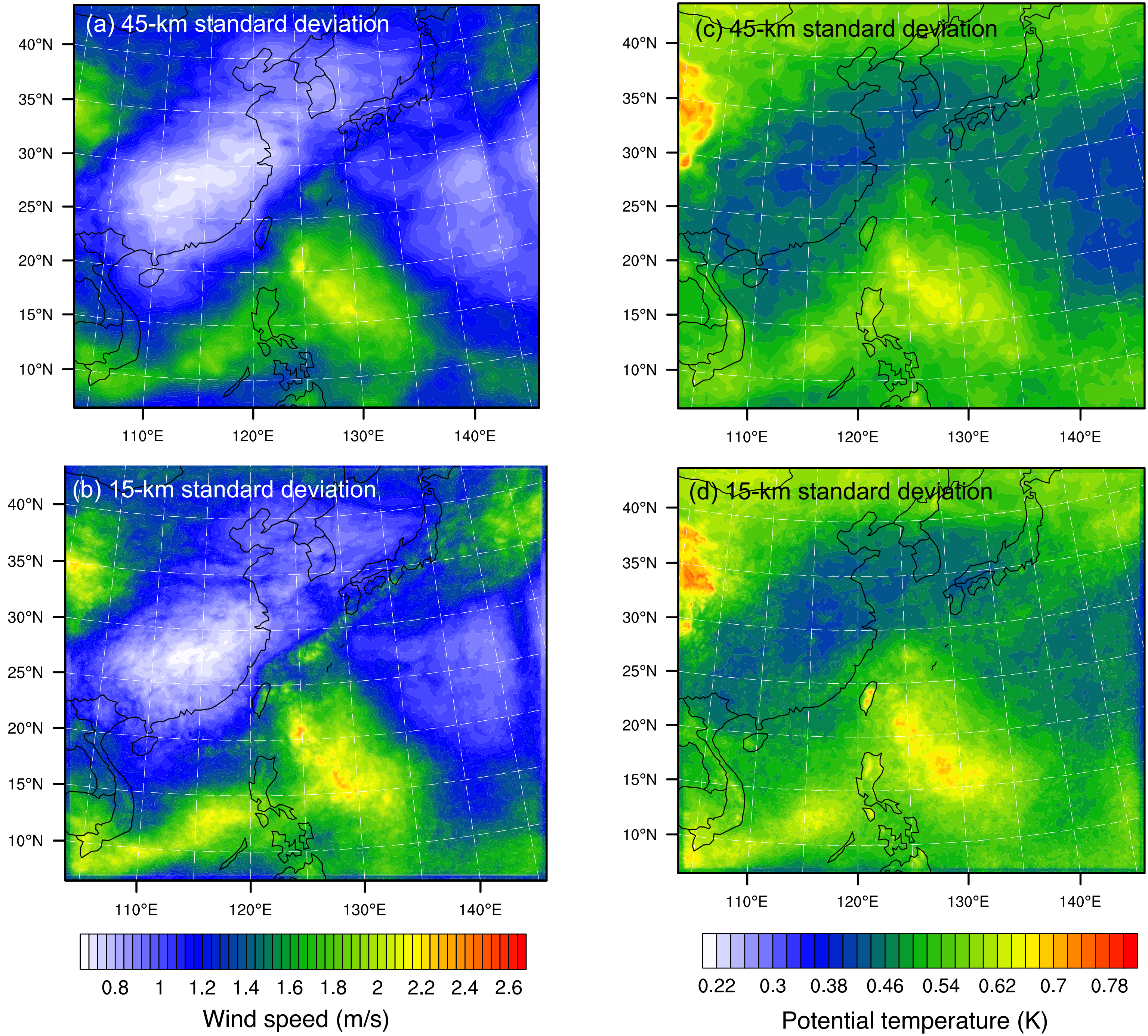

Fig. 10. Average prior ensemble standard deviation (spread) of 500 hPa (a,b) wind speed (m/s) and (c,d) potential temperature (K) between 1800 UTC 8 and 0000 UTC 28 September for the (a,c) 45- and (b,d) 15-km ensembles.

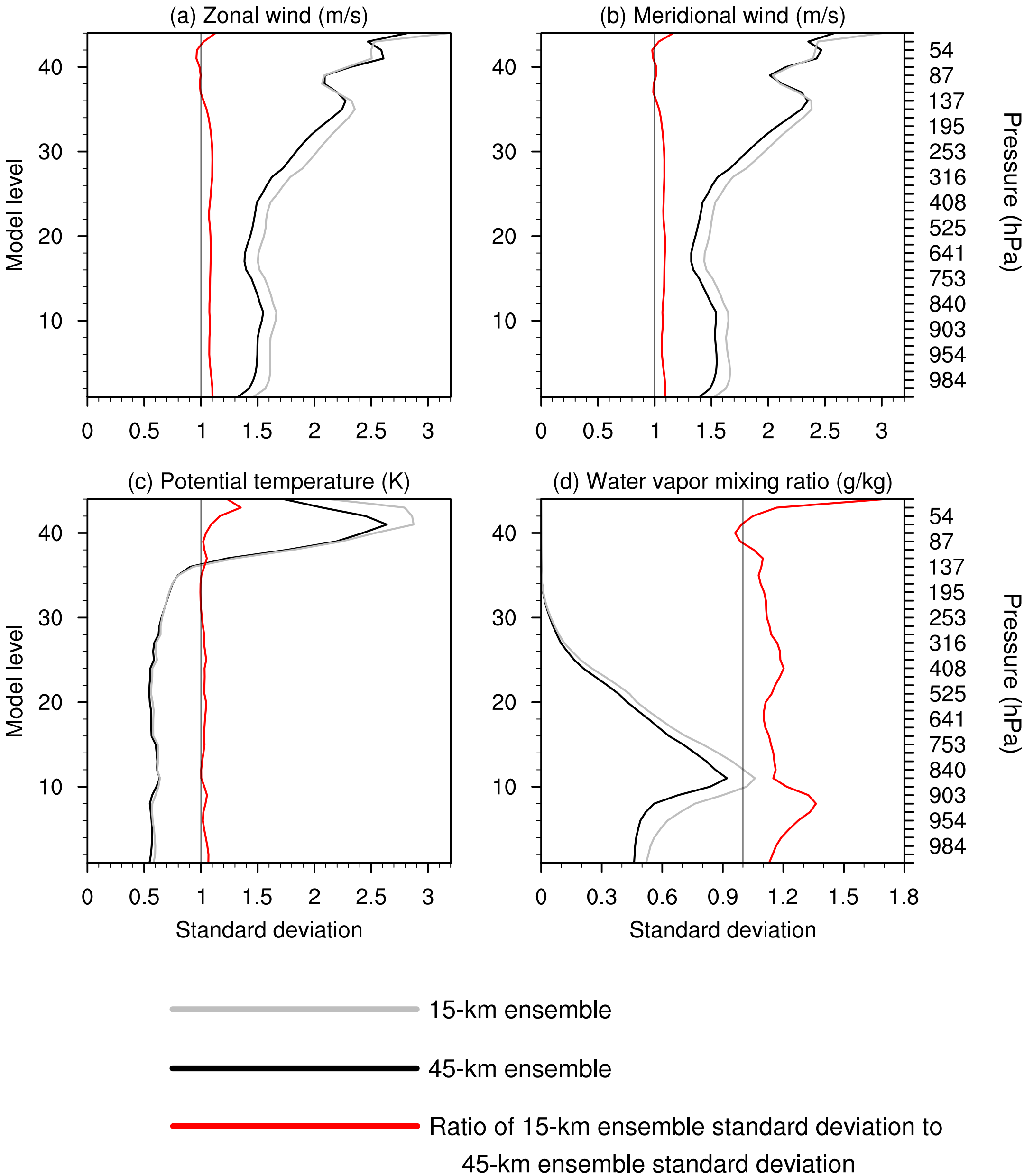

Fig. 11. Domain average prior ensemble standard deviations between 1800 UTC 8 and 0000 UTC 28 September for (a) zonal wind (m/s), (b) meridional wind (m/s), (c) potential temperature (K), and (d) water vapor mixing ratio (g/kg). The approximate pressures (hPa) of selected model levels are shown on the right axes of (b) and (d). The 45-km statistics were computed solely over the portion of the 45-km domain co-located with the 15-km domain.

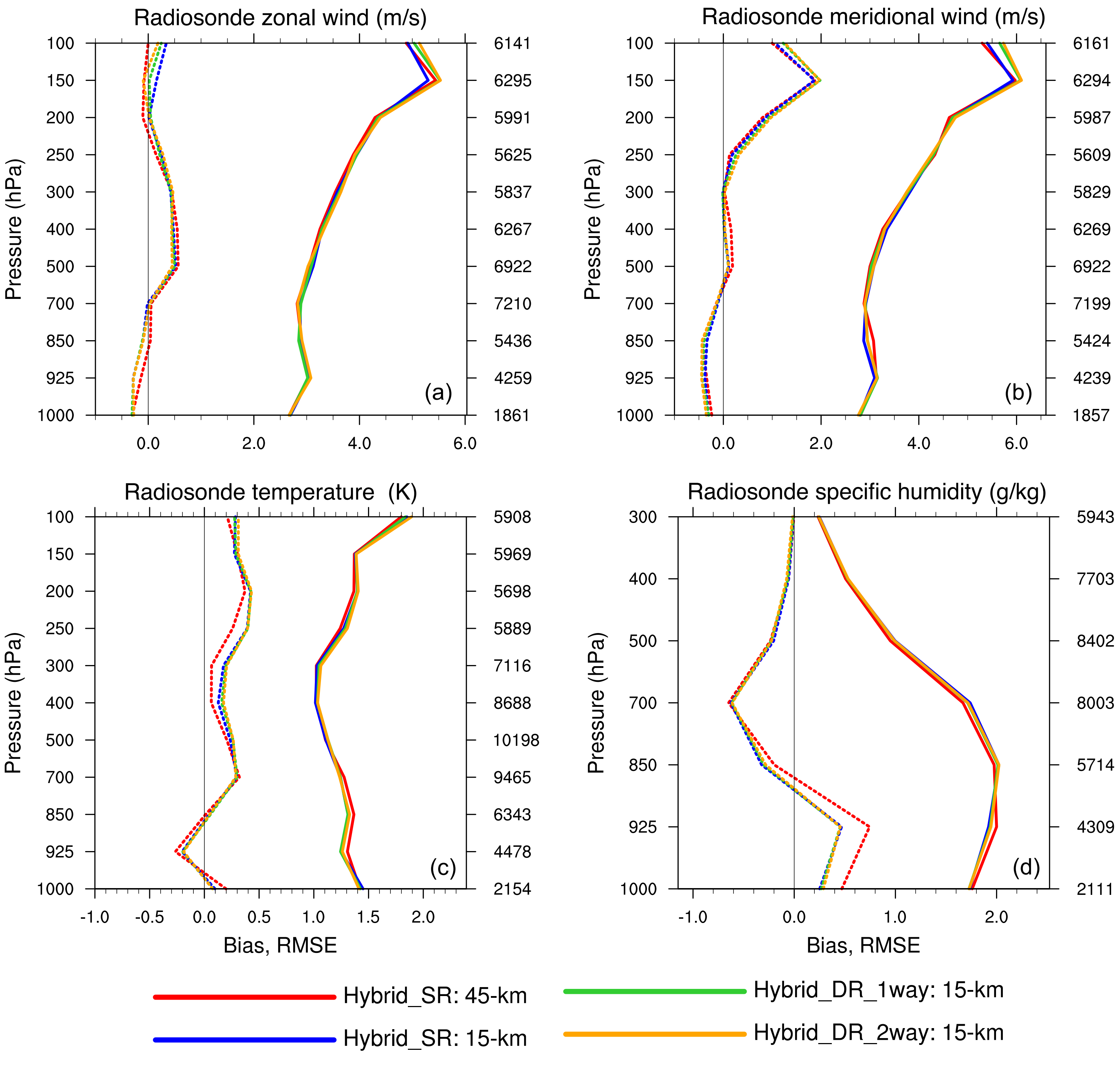

Fig. 12. RMSE (solid lines) and bias (dashed lines) for verification versus radiosonde (a) zonal wind (m/s), (b) meridional wind (m/s), (c) temperature (K), and (d) specific humidity (g/kg) observations averaged over all backgrounds (6-hr forecasts) between 1800 UTC 8 and 0000 UTC 28 September. The sample size at each level is denoted to the right of each panel.

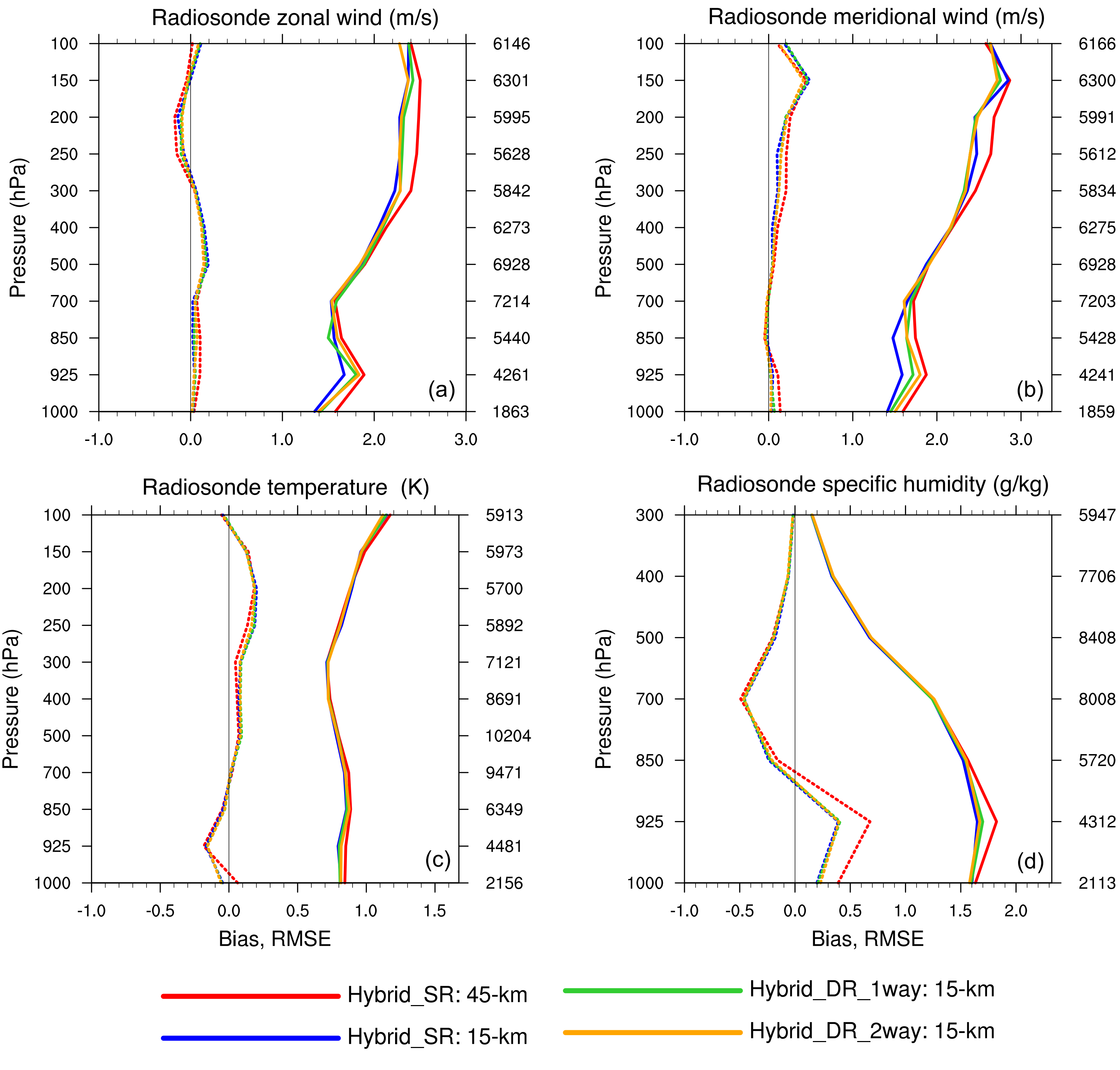

Fig. 13. As in Fig. 12 but for the mean analysis fits to observations.

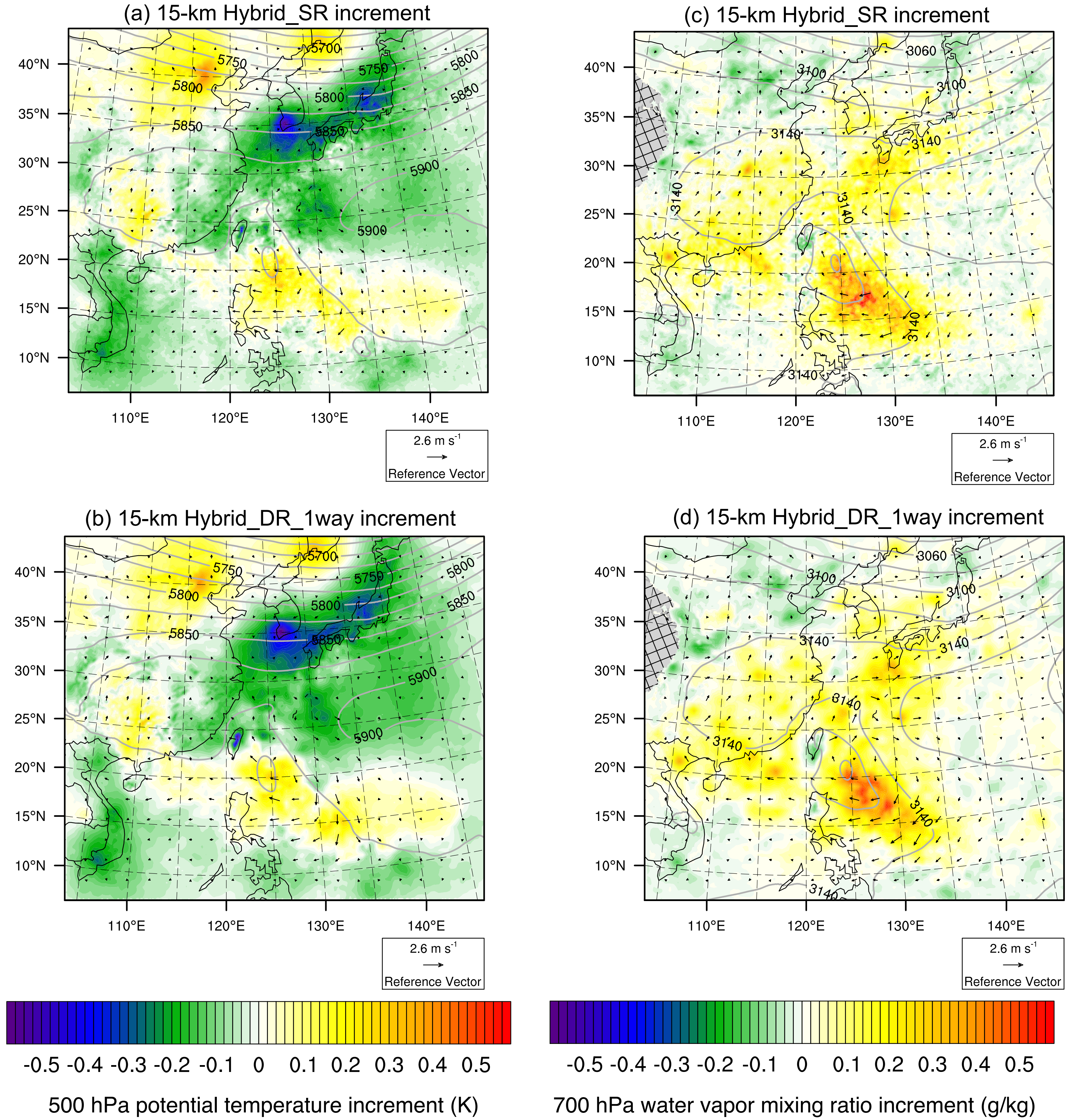

Fig. 14. 15-km 500 hPa potential temperature analysis increments (K), wind vector increments (arrows), and mean background 500 hPa height (m) averaged between 1800 UTC 8 and 0000 UTC 28 September for (a) Hybrid_SR and (b) Hybrid_DR_1way. (c,d) As in (a,b) except for 700 hPa water vapor mixing ratio increments (g/kg), wind vector increments, and mean background height. Hatching in (c) and (d) indicates those areas where the 700 hPa surface was underground. Heights are contoured every 20 meters in (a,b) and every 10 meters in (c,d).

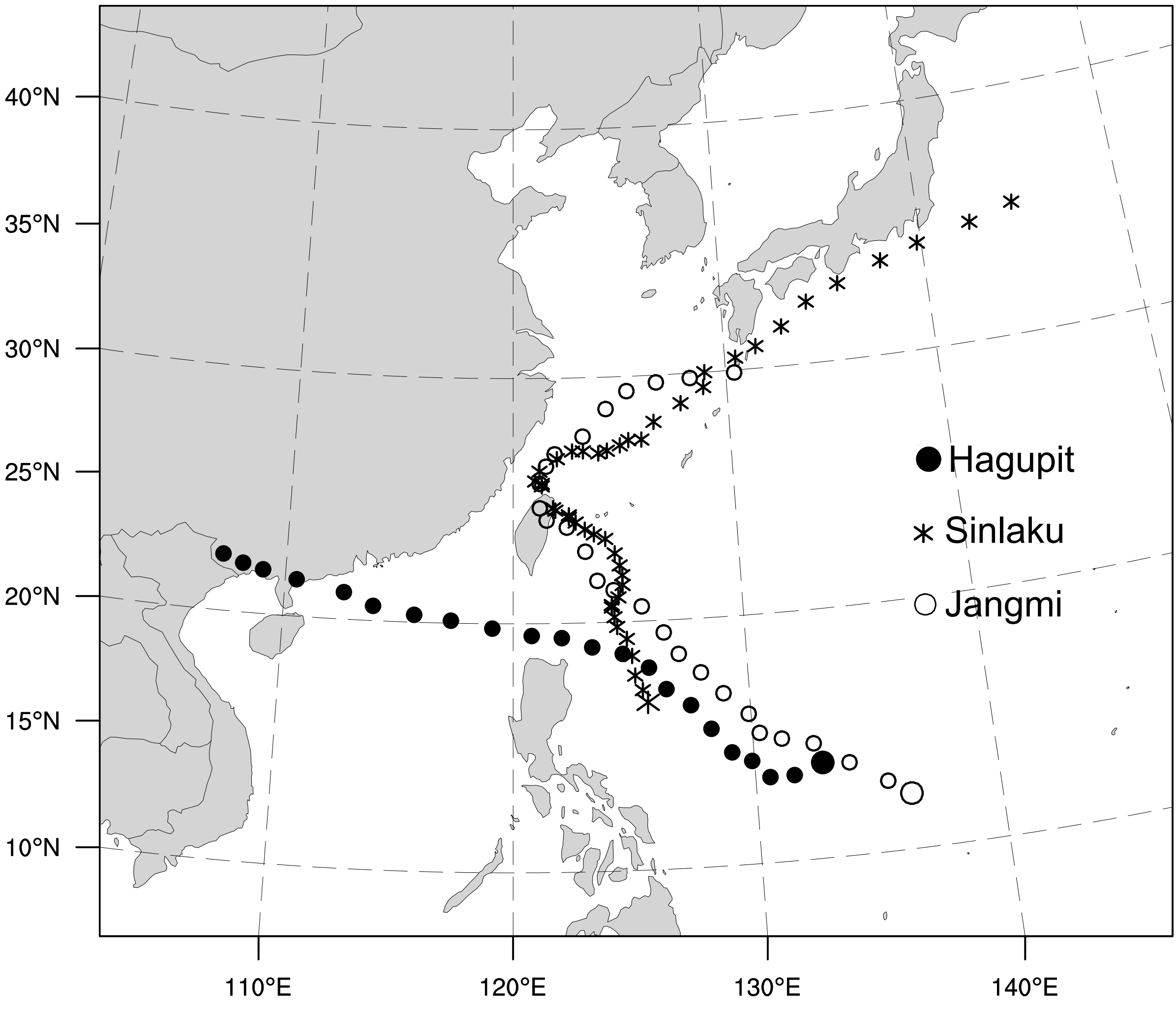

Fig. 15. (a) Best track positions of tropical cyclones Sinlaku, Hagupit, and Jangmi. Locations are plotted every 6-hrs. See Table 3 for the starting and ending times of each storm.

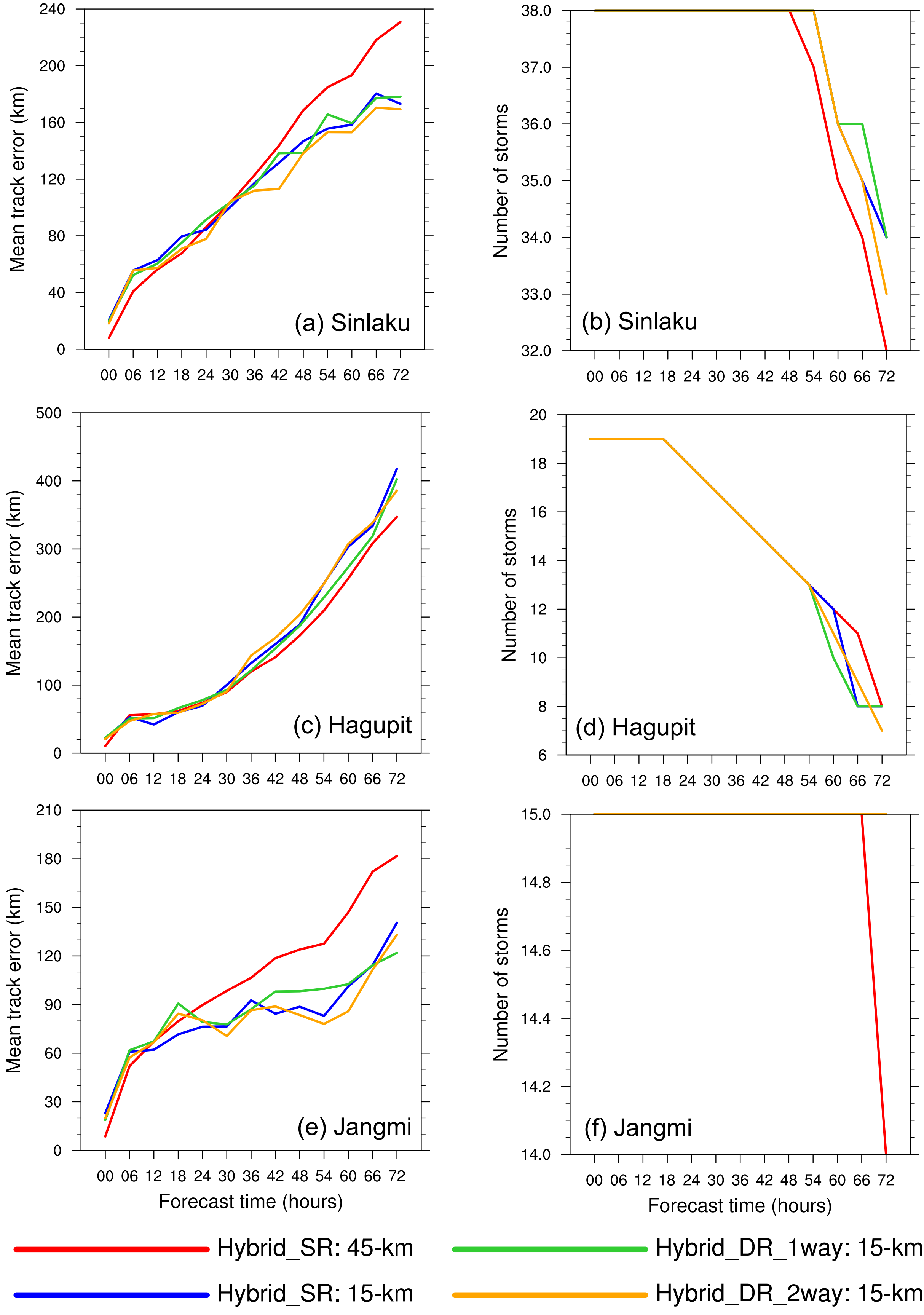

Fig. 16. Mean 0-72-hr absolute track errors (km) and sample sizes for (a,b) Sinlaku, (c,d) Hagupit, and (e,f) Jangmi.

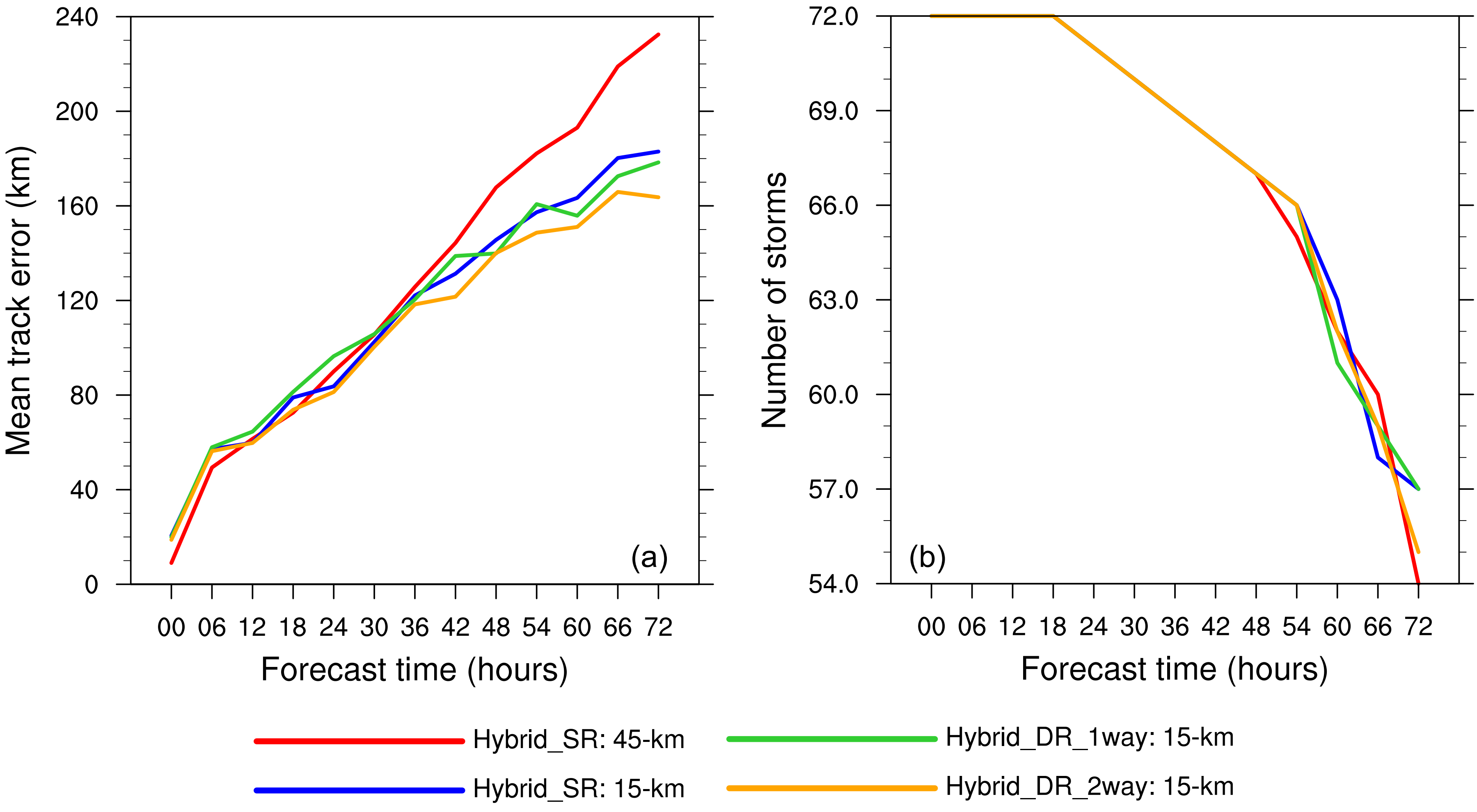

Fig. 17. As in Fig. 16 but track errors averaged over the three TCs and the total sample size.

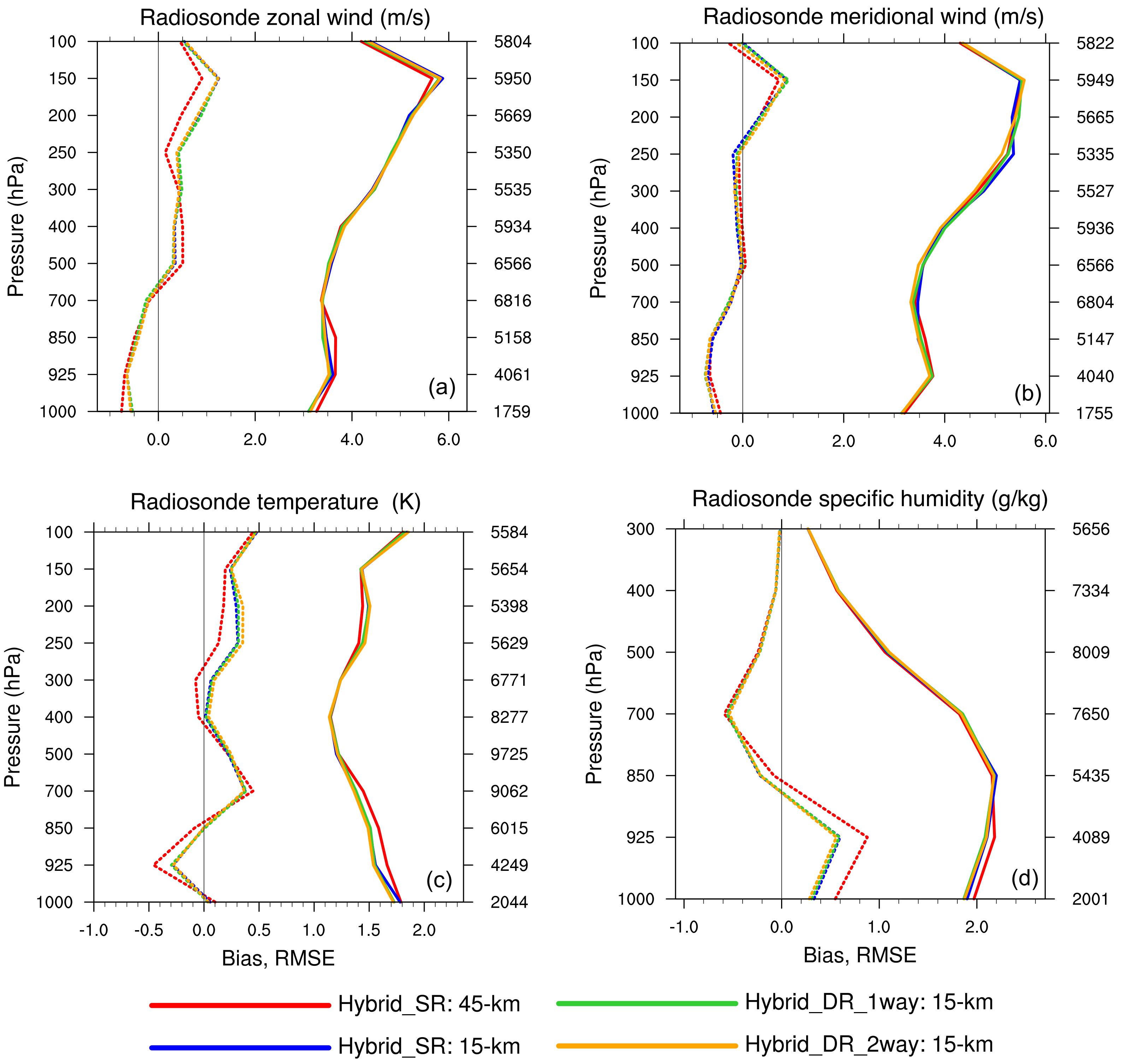

Fig 18. Average RMSE (solid lines) and bias (dashed lines) for verification of 24-hr forecasts versus radiosonde (a) zonal wind (m/s), (b) meridional wind (m/s), (c) temperature (K), and (d) specific humidity observations averaged over all 24-hr forecasts. The sample size at each level is denoted to the right of each panel.

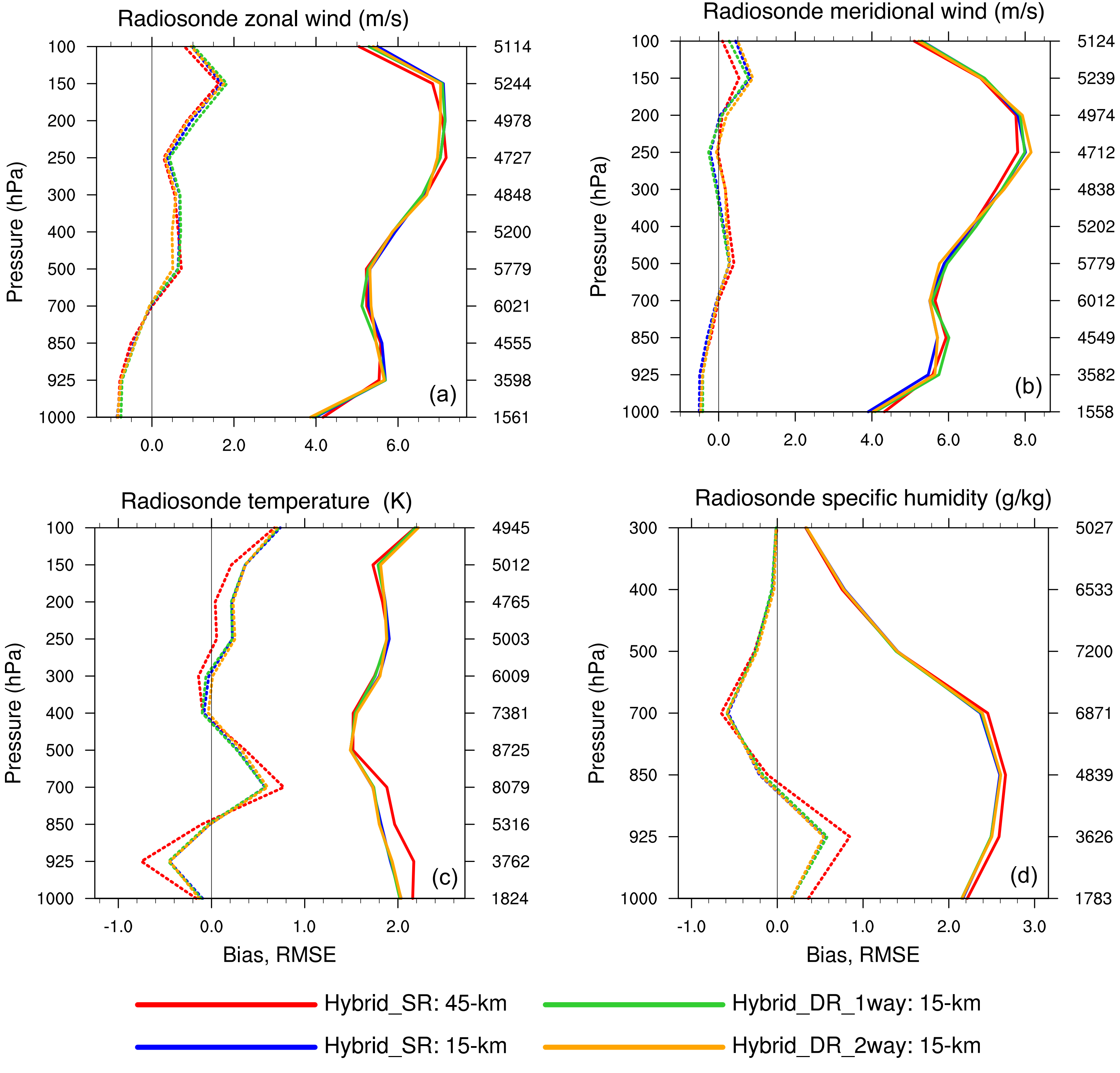

Fig. 19. As in Fig. 18 but for 72-hr forecasts.